

SANDIA REPORT

SAND2015-0132

Unlimited Release

Printed January 2015

The Science of Battery Degradation

John P. Sullivan, Kyle R. Fenton, Farid El Gabaly Marquez, C. Tom Harris, Carl C. Hayden, Nicholas S. Hudak, Katherine L. Jungjohann, Christopher J. Kliwer, Kevin Leung, Kevin McCarty, Anthony H. McDaniel, Ganesan Nagasubramanian, Joshua D. Sugar, Alec A. Talin, Craig M. Tenney, Kevin R. Zavadil

Prepared by
Sandia National Laboratories
Albuquerque, New Mexico 87185 and Livermore, California 94550

Sandia National Laboratories is a multi-program laboratory managed and operated by Sandia Corporation, a wholly owned subsidiary of Lockheed Martin Corporation, for the U.S. Department of Energy's National Nuclear Security Administration under contract DE-AC04-94AL85000.

Approved for public release; further dissemination unlimited.



Sandia National Laboratories

Issued by Sandia National Laboratories, operated for the United States Department of Energy by Sandia Corporation.

NOTICE: This report was prepared as an account of work sponsored by an agency of the United States Government. Neither the United States Government, nor any agency thereof, nor any of their employees, nor any of their contractors, subcontractors, or their employees, make any warranty, express or implied, or assume any legal liability or responsibility for the accuracy, completeness, or usefulness of any information, apparatus, product, or process disclosed, or represent that its use would not infringe privately owned rights. Reference herein to any specific commercial product, process, or service by trade name, trademark, manufacturer, or otherwise, does not necessarily constitute or imply its endorsement, recommendation, or favoring by the United States Government, any agency thereof, or any of their contractors or subcontractors. The views and opinions expressed herein do not necessarily state or reflect those of the United States Government, any agency thereof, or any of their contractors.

Printed in the United States of America. This report has been reproduced directly from the best available copy.

Available to DOE and DOE contractors from

U.S. Department of Energy
Office of Scientific and Technical Information
P.O. Box 62
Oak Ridge, TN 37831

Telephone: (865) 576-2087
Facsimile: (865) 576-5728
E-Mail: reports@adonis.osti.gov
Online ordering: <http://www.osti.gov/bridge>

Available to the public from

U.S. Department of Commerce
National Technical Information Service
5301 Shawnee Rd
Alexandria, VA 22312

Telephone: (800) 553-6847
Facsimile: (703) 605-6900
E-Mail: orders@ntis.gov
Online order: <http://www.ntis.gov/help/ordermethods.aspx#online>



SAND2015-0132
Unlimited Release
January 2015

The Science of Battery Degradation

John P. Sullivan, Farid El Gabaly, Kevin McCarty, Joshua D. Sugar, and Alec A. Talin
Materials Physics
Sandia National Laboratories
P.O. Box 969
Livermore, California 94551-9161

Kyle R. Fenton and Ganesan Nagasubramanian
Power Sources Design and Development
Sandia National Laboratories
P.O. Box 5800
Albuquerque, New Mexico 87185-0614

C. Tom Harris and Katherine L. Jungjohann
Nanosystems Synthesis/Analysis
Sandia National Laboratories
P.O. Box 5800
Albuquerque, New Mexico 87185-1304

Carl C. Hayden and Christopher J. Kliever
Combustion Chemistry Dept.
Sandia National Laboratories
P.O. Box 969
Livermore, CA 94551-9055

Nicholas S. Hudak
Power Sources Research and Development
Sandia National Laboratories
P.O. Box 5800
Albuquerque, New Mexico 87185-0613

Kevin Leung
Nanostructure Physics
Sandia National Laboratories
P.O. Box 5800
Albuquerque, New Mexico 87185-1415

Anthony H. McDaniel
Hydrogen and Combustion Technology

Sandia National Laboratories
P.O. Box 969
Livermore, California 94551-9052

Craig M. Tenney
Chemical and Biological Systems
Sandia National Laboratories
P.O. Box 5800
Albuquerque, New Mexico 87185-0754

Kevin R. Zavadil
Advanced Materials Laboratory
Sandia National Laboratories
P.O. Box 5800
Albuquerque, New Mexico 87185-0888

Abstract

This report documents work that was performed under the Laboratory Directed Research and Development project, Science of Battery Degradation. The focus of this work was on the creation of new experimental and theoretical approaches to understand atomistic mechanisms of degradation in battery electrodes that result in loss of electrical energy storage capacity. Several unique approaches were developed during the course of the project, including the invention of a technique based on ultramicrotoming to cross-section commercial scale battery electrodes, the demonstration of scanning transmission x-ray microscopy (STXM) to probe lithium transport mechanisms within Li-ion battery electrodes, the creation of in-situ liquid cells to observe electrochemical reactions in real-time using both transmission electron microscopy (TEM) and STXM, the creation of an in-situ optical cell utilizing Raman spectroscopy and the application of the cell for analyzing redox flow batteries, the invention of an approach for performing ab initio simulation of electrochemical reactions under potential control and its application for the study of electrolyte degradation, and the development of an electrochemical entropy technique combined with x-ray based structural measurements for understanding origins of battery degradation. These approaches led to a number of scientific discoveries. Using STXM we learned that lithium iron phosphate battery cathodes display unexpected behavior during lithiation wherein lithium transport is controlled by nucleation of a lithiated phase, leading to high heterogeneity in lithium content at each particle and a surprising invariance of local current density with the overall electrode charging current. We discovered using in-situ transmission electron microscopy that there is a size limit to lithiation of silicon anode particles above which particle fracture controls electrode degradation. From electrochemical entropy measurements, we discovered that entropy changes little with degradation but the origin of degradation in cathodes is kinetic in nature, i.e. lower rate cycling recovers lost capacity. Finally, our modeling of electrode-electrolyte interfaces revealed that electrolyte degradation may occur by either a single or double electron transfer process depending on thickness of the solid-electrolyte-interphase layer, and this cross-over can be modeled and predicted.

CONTENTS

1. Introduction.....	9
1.1. References.....	12
2. In-situ Transmission Electron Microscopy.....	13
2.1. Advancing state-of-the-art <i>in-situ</i> TEM for battery electrochemistry	13
2.2. Analytic TEM of battery cathodes.....	14
2.3. Quantitative electrochemistry inside the TEM	15
2.4. References.....	16
3. Scanning Transmission X-ray Microscopy	19
3.1. STXM analysis of the lithiation process in LiFePO_4	19
3.2. STXM study of charging rate effects in LiFePO_4	20
3.3. References.....	21
4. In-Situ Liquid Cells	23
4.1. Abstract.....	23
4.2. Introduction.....	23
4.3. Liquid cell design and fabrication	24
4.3.1. Liquid Cell Design	24
4.3.2. Fabrication.....	26
4.4. Material placement	27
4.5. Quantitative electrochemistry considerations.....	28
4.6. Demonstration: <i>Operando</i> copper electrodeposition.....	30
4.7. Conclusion	33
4.8. Acknowledgment.....	33
4.9. References.....	33
5. Electrochemical Measurements	37
5.1. Abstract.....	37
5.2. Introduction.....	37
5.3. Methods	39
5.4. Results and Discussion	40
5.4.1. Entropy Measurement Technique and Data Analysis	40
5.4.2. Thermodynamic Profile of Li_xCoO_2	42
5.4.3. Effect of Fast Cycling	45
5.4.4. Effect of Slow Cycling.....	46
5.4.5. Cycling-Induced Changes in Entropy	48
5.5. Conclusion	49
5.6. Acknowledgements.....	50
5.7. References.....	51
6. Theory and Modeling	53
6.1. First principles investigation of the reduction of ethylene carbonate.....	53
6.2. First principles simulation of voltage-dependent electrochemistry in Li-ion batteries	54
6.3. References.....	55

7. Ongoing and future work.....	57
7.1. In situ TEM and STXM using Li-ion battery chemistry	57
7.2. In situ optical cells and optical characterization of flow batteries.....	58
7.3. Degradation studies of $\text{LiNi}_{0.5}\text{Co}_{0.2}\text{Mn}_{0.3}\text{O}_2$	59
7.4. References.....	61
Appendix A: Supplemental Information on Sandia's In-Situ TEM Liquid Cell.....	63
A.1. The Liquid Cell Discovery Platform: Imaging Electrochemical Processes in the Transmission Electron Microscope	63
A.1.1. Epoxy wicking to seal ring.....	63
A.1.2. Fabrication workflow	63
A.1.3. Post-processing lithography	64
A.1.4. Cell liquid filling	64
A.1.5. Electron beam energy loss in liquid	65
A.2. References.....	65
Distribution	67

FIGURES

Figure 1.1. Schematic representations of proposed degradation mechanisms	10
Figure 2.1. In-situ TEM images	13
Figure 2.2. High resolution TEM images.	14
Figure 2.3. Schematic of the ultramicrotoming method	15
Figure 2.4. An energy-filtered TEM image of LiFePO_4	15
Figure 2.5. Charge-discharge curves for a Si nanowire anode	16
Figure 3.1. State-of-charge mapping obtained via scanning transmission X-ray microscopy	20
Figure 3.2. Experiment and simulation of the fraction of actively lithiating LFP	21
Figure 4.1. Schematic render of the liquid cell.....	25
Figure 4.2. Optical micrograph of the bottom chip	26
Figure 4.3. Material assembly and patterning on electrode tips.	27
Figure 4.4. Limiting steady-state current.....	29
Figure 4.5. BF STEM image of two electrodes	32
Figure 4.6. Linear sweep voltammetry of Cu electrodeposition.	32
Figure 5.1. Typical data obtained for a dE/dT (entropy) measurement.....	42
Figure 5.2. Thermodynamic quantities measured as a function of the state-of-charge	43
Figure 5.3. Specific (gravimetric) capacity of galvanostatically cycled half-cells.....	44
Figure 5.4. Open-circuit potential and dE/dT of half-cells.....	44
Figure 5.5. Specific (gravimetric) capacity of galvanostatically cycled cells.	46
Figure 5.6. Open-circuit potential and dE/dT of half-cells.....	47
Figure 5.7. Thermodynamic data for LiCoO_2	47
Figure 5.8. Detail of the LiCoO_2 thermodynamic data.....	48
Figure 6.1. Different SEI formation regimes.....	53
Figure 6.2. Predicted potential ($-\Delta G_t/ e $) for virtual Li^+ transfer.....	54
Figure 7.1. Plating and stripping of Li metal on Ti electrodes	57
Figure 7.2. STXM image taken near the Fe absorption edge of LiFePO_4	58

Figure 7.3. An in situ optical cell for Raman spectroscopy of batteries.....	59
Figure 7.4. In situ Raman spectroscopy of vanadium trisdithiolene flow batteries	59
Figure 7.5. X-ray absorption spectra near the Mn absorption edge.....	60
Figure 7.6. A simulation cell of 6 layers of $\text{LiNi}_{0.5}\text{Co}_{0.2}\text{Mn}_{0.3}\text{O}_2$	60
Figure 7.7. Raman map of $\text{LiNi}_{0.5}\text{Co}_{0.2}\text{Mn}_{0.3}\text{O}_2$	61
Figure S1. Optical microscope image of bottom and top chips.....	63
Figure S2. Microfabrication steps used to fabricate the bottom chip of the liquid cell.....	64
Figure S3. A fully-assembled liquid cell being filled with liquid	65

TABLES

Table 1.1 Summary of Techniques	10
---------------------------------------	----

1. INTRODUCTION

The Dept. of Energy has identified the transformation of our nation's energy systems towards clean energy technologies as its first mission statement goal.[1] Electrical energy storage in the form of batteries is a key component of this vision. Current battery technologies need substantial improvements in capacity and lifetime in order to significantly reduce our dependence on fossil fuels and to increase the utilization of renewable energy sources on the nation's electrical grid. While there has been much work and investment in new materials to improve capacity, the understanding of how to improve lifetime has lagged. The objective of this project was to create new techniques that are capable of probing, down to the atomic level, the leading mechanism(s) that give rise to battery degradation.

All batteries degrade over time with or without cycling as manifested by a loss in total storage capacity. This degradation is near-universally attributed to "processes" at the electrode/electrolyte interfaces, but these "processes" are not well-described. In Tarascon's highly-cited review of Li-ion batteries he states the need for fundamental studies, "The principal challenge for Li based rechargeable batteries, or indeed for any battery, lies in gaining better understanding and control of the electrode-electrolyte interface ... the main difficulty stems from a lack of available techniques to probe the evolution of the electrode-electrolyte interface at a local level." [2] Without this understanding, many models of battery degradation simply invoke a continuous loss of Li through side reactions, mostly at the anode, which are presumed to be a result of the continuous formation of the solid electrolyte interphase, SEI.[3] While it is certainly true that SEI formation will spontaneously occur on a Li-ion battery anode when lithiated, this layer should self-limit as the electron transport rate decreases.[4] Experimental or theoretical techniques that permit detailed understanding or direct experimental observation of the formation and continuous growth and/or dissolution of the SEI with battery cycling is an important goal.

There are several mechanisms that are believed to contribute to battery degradation (defined as an irreversible loss of battery capacity), and some of these are shown schematically in Fig. 1.1.[5],[6] Many models invoke a process of continuous SEI formation whether by formation and dissolution (Fig. 1.1a) or by mechanical failure of the SEI from cracking and/or delamination (Fig. 1.1b). At high charging rates or high cell impedance, Li plating may occur which will lead to further growth of SEI (Fig. 1.1c). It is also possible that degradation arises from mechanisms not related to SEI formation, such as the stranding of active particles (loss of electrical contact to a particle), Fig. 1.1d, or the blocking of electrolyte channels by precipitates or gas bubbles, Fig. 1.1e. Furthermore, for materials such as manganese oxide-based cathodes, there may be dissolution of the active particle, or phase changes may occur that reduce the particle's capacity to store Li or impede lithiation, Fig. 1.1f.

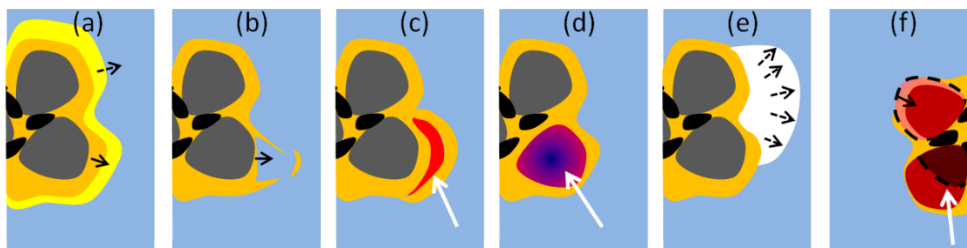


Figure 1.1. Schematic representations of proposed degradation mechanisms (gray is anode particle, black is binder/carbon conductor, dark red is cathode particle, orange is SEI, blue is electrolyte): (a) SEI growth (and dissolution), (b) SEI delamination followed by regrowth, (c) Li plating (white arrow) and SEI growth, (d) active particle stranding (white arrow), (e) blocking of electrolyte channels by precipitates or gas bubbles, and (f) active particle dissolution or phase change (white arrow)

To provide new and detailed understanding of the mechanisms of degradation that are operative in technologically-relevant Li-ion batteries, we developed several new techniques and approaches within this project. These approaches are summarized in Table 1.1 (below) and in the following sections of this Report. In those cases where our work has already appeared in print, we provide only a brief description of that work and refer the reader to the cited reference.

Table 1.1: Summary of Techniques Developed in this Project

Type	Description	Publications
TEM	In-situ TEM	<ol style="list-style-type: none"> 1. X. H. Liu, et al, "Size-Dependent Fracture of Silicon Nanoparticles During Lithiation," <i>ACS Nano</i> 6, 1522 (2012). 2. X. H. Liu, et al., "In situ atomic scale imaging of electrochemical lithiation of silicon," <i>Nature Nanotech</i> 7, 749 (2012). 3. W. Liang, et al., "Tough Germanium Nanoparticles under Electrochemical Cycling," <i>ACS Nano</i> 7, 3427 (2013). 4. Y. Liu, et al., "Tailoring Lithiation Behavior by Interface and Bandgap Engineering at the Nanoscale," <i>Nano Lett.</i> 13, 4876 (2013). 5. K. E. Gregorczyk, et al., "In Situ Transmission Electron Microscopy Study of Electrochemical Lithiation and Delithiation Cycling of the Conversion Anode RuO_2," <i>ACS Nano</i> 7, 6354 (2013). 6. Y. Zhu, et al., "In Situ Atomic-Scale Imaging of Phase Boundary Migration in FePO_4 Microparticles during Electrochemical Lithiation," <i>Adv. Mater.</i> 25, 5461 (2013).
	Analytic TEM	<ol style="list-style-type: none"> 1. J. D. Sugar, et al., "High-Resolution Chemical Analysis on Cycled LiFePO_4 Battery Electrodes Using Energy-Filtered TEM." <i>J. Power Sources</i> 246, 512 (2013).

	Quantitative electrochemistry inside a TEM	1. K. Zavadil, et al., "In situ TEM cycling of Si anodes under current control," to be submitted (2014).
Scanning Transmission X-ray Microscopy	STXM	1. W. C. Chueh, et al., "Intercalation Pathway in Many-Particle LiFePO ₄ Electrode Revealed by Nanoscale State-of-Charge Mapping," <i>Nano Lett.</i> 13 , 866 (2013). 2. Y. Li, et al., "Current-induced transition from particle-by-particle to concurrent intercalation in phase-separating battery electrodes," <i>Nature Mater.</i> 13 , 1149 (2014). 3. F. El Gabaly, et al., "STXM studies of LiNi _{0.5} Co _{0.2} Mn _{0.3} O ₂ ," ongoing work, 2014.
	In Situ STXM	1. F. El Gabaly, et al., "In Situ STXM of LiFePO ₄ ," ongoing work, 2014.
MEMS Discovery Platform	MEMS liquid cell	1. A. J. Leenheer, et al., "A Sealed Liquid Cell for in-situ Transmission Electron Microscopy of Controlled Electrochemical Processes," accepted in <i>J. MEMS</i> (2014). 2. A. J. Leenheer, et al., "Lithium electrodeposition dynamics imaged in-situ by liquid cell scanning transmission electron microscopy," manuscript in preparation, 2014.
Optical	Raman mapping	1. C. Hayden, and A. A. Talin, "Raman spectroscopic analysis of LiNi _{0.5} Co _{0.2} Mn _{0.3} O ₂ cathodes stressed to high voltage," manuscript in preparation, 2014.
	In situ Raman	1. A. Talin et al., "In situ Raman of a Vanadium Trisdithiolene redox flow battery," manuscript in preparation, 2014.
Electro-chemical	Electrochemical entropy	1. N. S. Hudak, et al., "Cycling-Induced Changes in the Entropy Profiles of Lithium Cobalt Oxide Electrodes," accepted for publication in <i>J. Electrochem. Soc.</i> (2014).
Theory and modeling	First principles theory of electrode/electrolyte interfaces	1. K. Leung, "Two-electron reduction of ethylene carbonate: A quantum chemistry re-examination of mechanisms" <i>Chem. Phys. Lett.</i> 568-569 , 1 (2013). 2. K. Leung et al., "Toward First Principles Prediction of Voltage Dependences of Electrolyte/Electrolyte Interfacial Processes in Lithium Ion Batteries," <i>J. Phys. Chem C</i> 117 , 24224 (2013).
	Theory and simulation of NMC cathodes	1. A. H. McDaniel, et al., "X-ray absorption analysis of LiNi _{0.5} Co _{0.2} Mn _{0.3} O ₂ as a function of state-of-charge," ongoing work, 2014.

1.1. References

- [1] <http://www.energy.gov/about/index.htm>
- [2] J.-M Tarascon and M. Armand, *Nature* **414**, 359 (2001).
- [3] J. Christensen and J. Newman, *J. Electrochem. Soc.* **150**, A1416 (2003).
- [4] K. Xu, *Chem. Rev.* **104**, 4303 (2004).
- [5] P. Arora, R. E. White, and M. Doyle, *J. Electrochem. Soc.* **145**, 3647 (1998).
- [6] M. Broussely, Ph. Biensan, F. Bonhomme, Ph. Blanchard, S. Herreyre, K. Nechev, and R. J. Staniewicz, *J. Power Sources* **146**, 90 (2005).

2. IN-SITU TRANSMISSION ELECTRON MICROSCOPY

Transmission electron microscopy (TEM) and, in particular, in-situ TEM have proven to be very valuable techniques to observe and analyze nanoscale and atomistic mechanisms associated with battery electrode lithiation, delithiation, cycling, mechanical fatigue and failure. Following from the initial work of Huang et al. that demonstrated the technique of in-situ TEM measurements for real-time lithiation of Li-ion battery anodes[Huang], this TEM capability was expanded in this project in four significant areas: 1. Refining the spatial resolution to the atomic-scale and observing lithiation mechanisms through several charge-discharge cycles, 2. Introducing a new approach to section battery electrodes using ultramicrotoming and demonstrating advanced analytic TEM techniques that provide chemical sensitivity, 3. Coupling TEM observations with sensitive electrochemical instruments for performing quantitative electrochemical measurements in situ, and 4. Creating a fully-functional liquid electrochemical cell for performing TEM observations through volatile electrolytes. In this section, we summarize publications developed in this project in the first three areas. We describe the development of the liquid TEM cell in Section 4.

2.1. Advancing state-of-the-art *in-situ* TEM for battery electrochemistry

One discovery that was made in this project is that the degradation mechanism of certain Li-ion battery electrodes is sensitive to the size of the active electrode particles.[1] Silicon is a Li-ion battery anode that is attractive for its high storage capacity, but anodes based on silicon typically show high degradation and short lifetime. Our TEM analysis showed a strong size dependence to silicon anode particle fracture: anode particles greater than 150 nm fracture upon lithiation whereas smaller particles do not (see Figure 2.1). Looking in detail at the lithiation mechanism of silicon, we observed that the lithiation of crystalline silicon occurs via a ledge mechanism wherein an amorphous Li_xSi alloy is formed through layer-by-layer peeling of $\{111\}$ atomic planes (see Figure 2.2).[2]

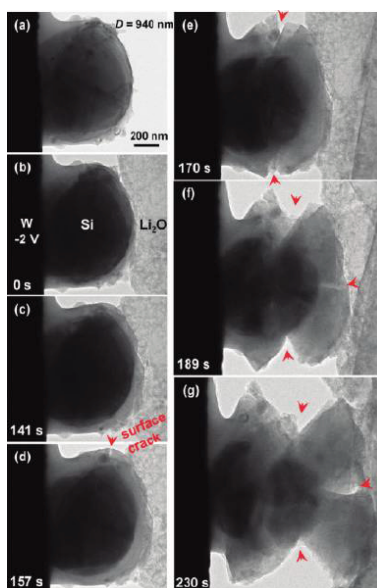


Figure 2.1. In-situ TEM images of ~1 micron diameter Si anode particle as it electrochemically alloys with Li. When the lithiated shell exceeds approximately 150 nm in thickness, cracks form which leads to particle pulverization.

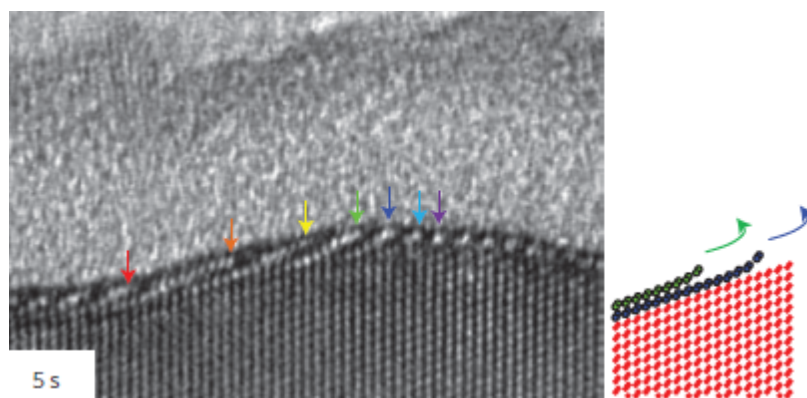


Figure 2.2. High resolution TEM images of a silicon anode as it electrochemically alloys with Li. The lithiation front advances by a ledge flow mechanism shown schematically on the right (field of view in the image is approximately 20 nm).

Other anode materials exhibit dramatically different behavior. For example, we observed that Ge anodes show less crystallographic anisotropy during lithiation compared to Si anodes, and this results in lower initial degradation.[3] The electronic structure of the anode also plays an important role in the lithiation mechanism. For example, we determined that the lithiation mechanism could be radically altered by creating a semiconductor heterojunction interface, e.g. a Si/Ge interface, that changes the electrical conductivity in the near-surface region.[4] Lastly, in-situ TEM was instrumental for explaining one of the mysteries associated with oxide-based anodes, specifically the high reversibility of RuO_2 anodes. Our study showed that reduced Ru metal nanoparticles are present in the lithiated oxide, and this provides electrical conductivity for the delithiation process.[5]

2.2. Analytic TEM of battery cathodes

The application of TEM and in-situ TEM is not limited to battery anode materials. Our initial work on investigating degradation mechanisms in cathodes focused on the LiFePO_4 cathode system, as this has the advantage that lithiation and delithiation occur via a phase change from the FePO_4 phase to the LiFePO_4 phase (in contrast, many common Li-ion battery cathodes that are oxide-based – such as LiCoO_2 – are insertion compounds where there is no change in crystal structure and little change in diffraction contrast over a large Li concentration range). In one study, we examined the atomic-scale mechanism for the lithiation of a FePO_4 particle using in-situ TEM where we found an atomically abrupt lithiation front with Li insertion along the $[010]$ lattice direction.[6]

In the examples presented above, we examined degradation mechanisms by looking at individual or small assemblages of active particles, but one of the goals in this project was to develop techniques that could be applied to realistic battery electrodes consisting of aggregates of active particles combined with conductive additives, polymeric binder, and the metallic current collectors. During the course of this project, we developed a method for sectioning full battery electrodes for later analysis by TEM or scanning transmission x-ray microscopy (a technique discussed in the next section). The method uses ultramicrotoming, which is a mechanical sectioning method employing diamond blades that cut strips from battery electrodes with

thicknesses as thin as 40 nm (see Figure 2.3). We employed this technique to examine the distribution of LiFePO_4 and FePO_4 particles in a battery electrode that had been cycled repeatedly and then polarized to 50% state-of-charge.[7] Using energy-filtered TEM (EF-TEM), maps of the lithiation states of the particle assemblies were created (see Figure 2.4) which compare favorably with STXM studies that are described in the next section.

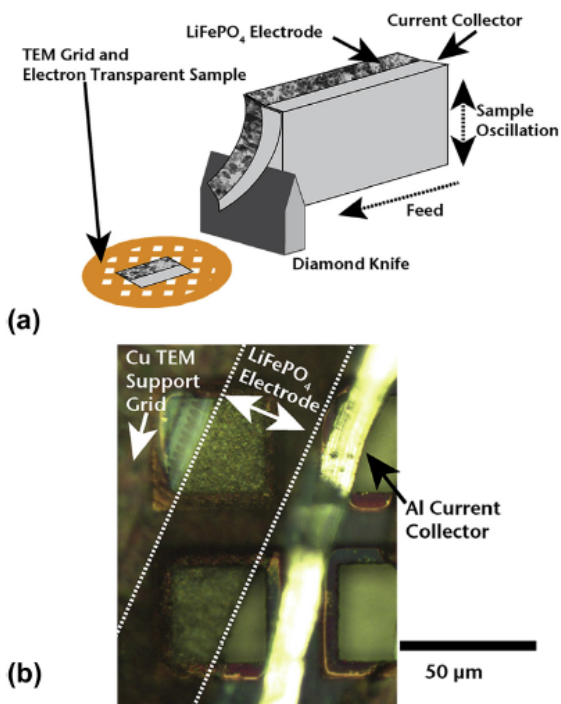


Figure 2.3. (a) Schematic of the ultramicrotomy method of preparing cross-sections from full battery electrodes for viewing by TEM. (b) One slice of battery electrode approximately 100 nm thick on a TEM grid.

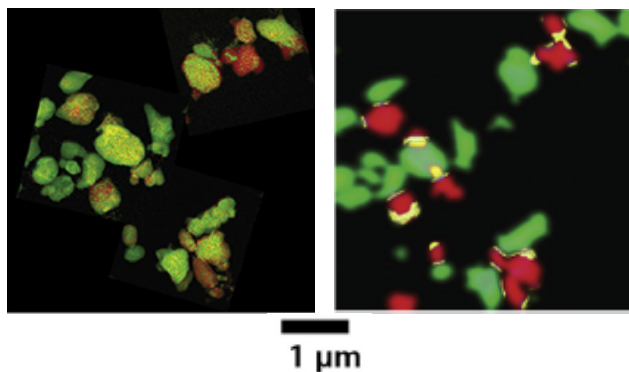


Figure 2.4. (left) An energy-filtered TEM image of LiFePO_4 cathode particles color coded where green is FePO_4 and red is LiFePO_4 . (right) A scanning transmission x-ray microscope image of the same region with the same color coding.

2.3. Quantitative electrochemistry inside the TEM

The identification of mechanisms that can lead to battery degradation in commercial scale batteries requires the electrodes to be electrochemically stressed similarly to real-use conditions. During electrochemical testing, one of the common measurement approaches is to perform chronopotentiometric sweeps under constant applied current, commonly called charge-discharge

cycling. One of the goals of this project was to develop techniques for performing quantitative charge-discharge electrochemical measurements during in-situ TEM. We demonstrated this technique using an experimental system consisting of a Si nanowire (NW) immersed in an ionic liquid electrolyte which offered the ability to accurately control the electrode area.[8] Figure 2.5 shows the initial charge-discharge cycle for a Si NW cycled with respect to a LiFePO₄ (LFP) cathode at a 5C rate. The dip in potential associated with nucleation of the lithiated silicon alloy is clearly visible, which highlights the value of assessing electrochemical behavior on a particle-by-particle basis, as opposed to averaging over an ensemble of particles. The charging current was a few pA (several orders of magnitude lower than typical laboratory-scale electrochemical testing), and this required the utilization of high sensitivity potentiostats and rigorous control of sources of current noise.

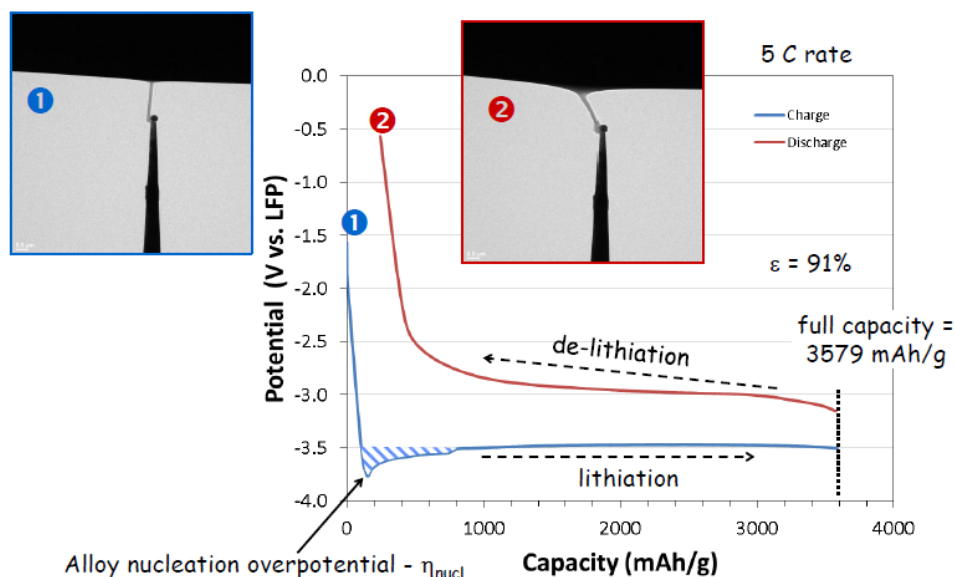


Figure 2.5. Charge-discharge curves for a Si nanowire anode cycled at constant current (constant charging rate) with respect to a LiFePO₄ counter electrode inside a TEM. The inset images show the nanomanipulator (thick needle), the Si nanowire (thin line) and the ionic liquid electrolyte (dark region).

2.4. References

1. X. H. Liu, L. Zhong, S. Huang, S. X. Mao, T. Zhu, J. Y. Huang, "Size-Dependent Fracture of Silicon Nanoparticles During Lithiation," *ACS Nano* **6**, 1522 (2012).
2. X. H. Liu, Y. Liu, J. Y. Huang, et al., "In situ atomic scale imaging of electrochemical lithiation of silicon," *Nature Nanotech* **7**, 749 (2012).
3. W. Liang, H. Yang, F. Fan, Y. Liu, X. H. Liu, J. Y. Huang, T. Zhu and S. Zhang, "Tough Germanium Nanoparticles under Electrochemical Cycling," *ACS Nano* **7**, 3427 (2013).
4. Y. Liu, X. H. Liu, B.-M. Nguyen, J. Yoo, J. P. Sullivan, S. T. Picraux, J. Y. Huang and S. A. Dayeh, "Tailoring Lithiation Behavior by Interface and Bandgap Engineering at the Nanoscale," *Nano Lett.* **13**, 4876 (2013).
5. K. E. Gregorczyk, Y. Liu, J. P. Sullivan and G. W. Rubloff, "In Situ Transmission Electron Microscopy Study of Electrochemical Lithiation and Delithiation Cycling of the Conversion Anode RuO₂," *ACS Nano* **7**, 6354 (2013).
6. Y. Zhu, J. W. Wang, Y. Liu, X. H. Liu, A. Kushima, Y. H. Liu, Y. Xu, S. X. Mao, J. Li, C. Wang and J. Y. Huang, "In Situ Atomic-Scale Imaging of Phase Boundary Migration in FePO₄ Microparticles during Electrochemical Lithiation," *Adv. Mater.* **25**, 5461 (2013).

7. J. D. Sugar, F. El Gabaly, W. Chueh, K. R. Fenton, T. Tyliczszak, P. G. Kotula, N. C. Bartelt. "High-Resolution Chemical Analysis on Cycled LiFePO_4 Battery Electrodes Using Energy-Filtered TEM." *J. Power Sources* **246**, 512 (2013).
8. K. Zavadil, Y. Liu, K. Jungjohann, "In situ TEM cycling of Si anodes under current control," to be submitted (2014).

3. SCANNING TRANSMISSION X-RAY MICROSCOPY

Transmission electron microscopy provides extremely high spatial resolution for resolving mechanisms of lithiation and degradation, but it suffers from limited chemical sensitivity when applied to thicker active electrode particles. Scanning transmission x-ray microscopy (STXM) is a technique that uses a highly collimated x-ray beam from a synchrotron light source in order to create an x-ray absorption map with approximately 20 nm spatial resolution of a thin sample. In this project, we developed a STXM capability for analyzing the local state-of-charge of cathode particles in a cross-section of a battery electrode that had been cycled through several charge-discharge cycles. The initial work focused on Li-ion battery cathodes based on LiFePO_4 (LFP), and the research goals were to both prove the technique and use the new approach to understand the mechanism of lithiation and lithium transport LFP cathodes.

3.1. STXM analysis of the lithiation process in LiFePO_4

Using the technique of ultramicrotoming to create thin slices of battery electrodes, described in section 2.2, thin slices of battery cathodes were extracted from coin cells consisting of an ~ 35 μm thick carbon-coated LFP/graphite composite cathode, Li anode, and 1.2 M LiPF_6 /ethylene carbonate/ethyl methyl carbonate electrolyte that were electrochemically cycled five times and stopped at 50% state-of-charge. These slices were examined using STXM at the Advanced Light Source, LBNL, where maps of x-ray absorption near the Fe K-edge were created. The analysis revealed that the overwhelming majority of particles were either almost completely delithiated or lithiated, the pattern of lithiation was not correlated with spatial position in the electrode (from the current collector to the electrode surface), and the probability of lithiation or delithiation was not strongly correlated to particle size (see Figure 3.1). The results unambiguously confirm a mosaic (particle-by-particle) pathway of intercalation and suggest that the rate limiting process of charging is the nucleation of the phase transformation.[1]

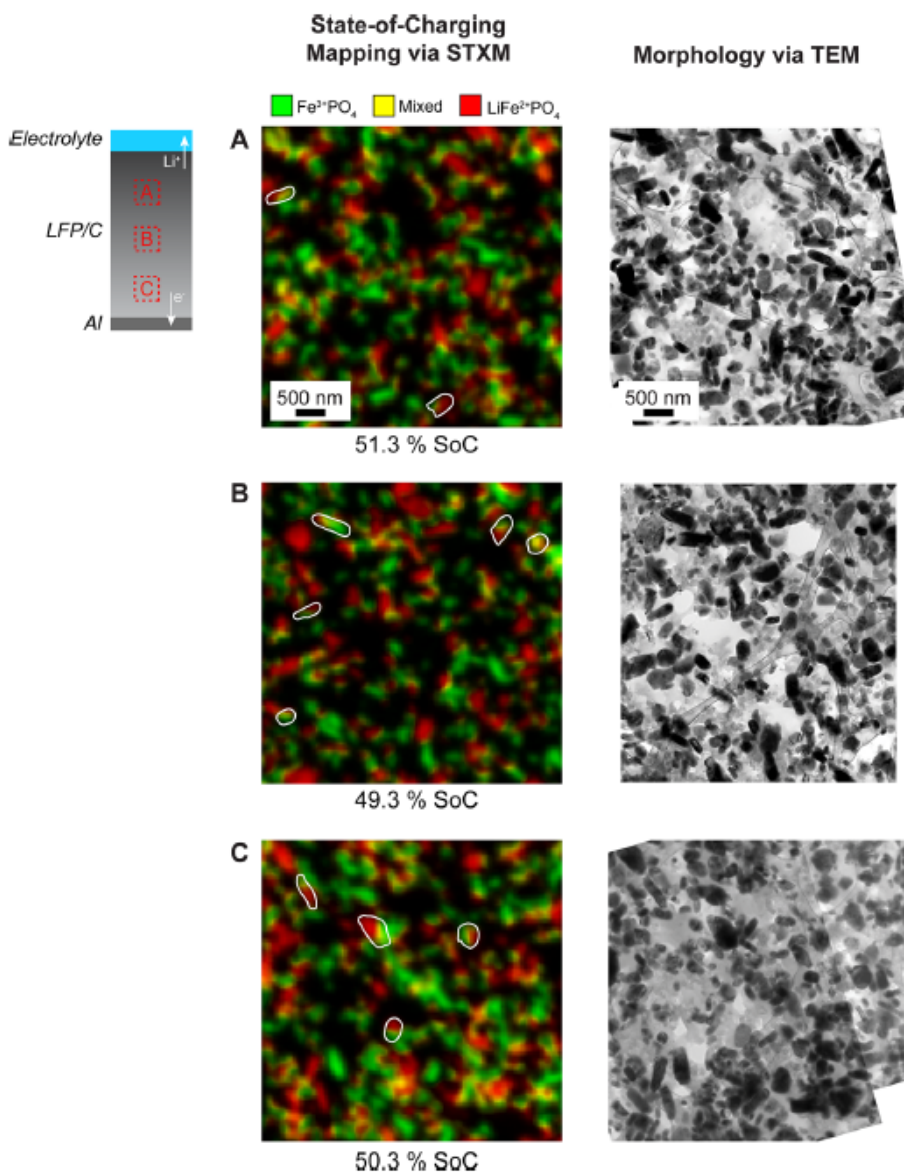


Figure 3.1. (Left) state-of-charge mapping obtained via scanning transmission X-ray microscopy and (right) morphology obtained via transmission electron microscopy of the same regions in the lithium iron phosphate composite electrode (A) 26 μm , (B) 18 μm (C) and 6 μm from the Al current collector.

3.2. STXM study of charging rate effects in LiFePO_4

In another STXM study, we examined the influence of charging rate on the lithiation behavior of LFP particles.[2] By probing the individual state-of-charge for over 3,000 LFP particles, we observed that the active population depended strongly on the cycling current, exhibiting particle-by-particle-like (sequential lithiation) behavior at low rates and increasingly concurrent (parallel lithiation) behavior at high rates. Also, contrary to intuition, the current density, or current per active internal surface area, is nearly invariant with the global electrode cycling rate. Rather, the electrode accommodates higher current by increasing the active particle population.

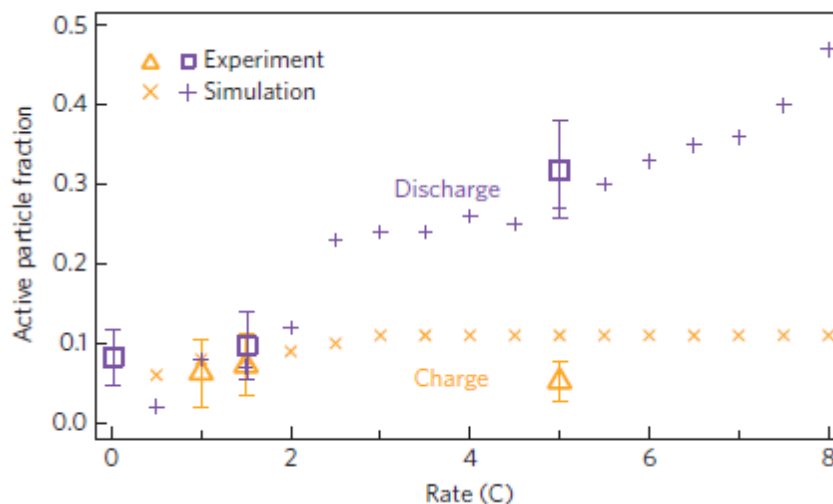


Figure 3.2. Experiment and simulation of the fraction of actively lithiating/delithiating LFP particles as a function of charging rate (C). Over these charging rates, the electrodes accommodates the extra charging or discharging current by increasing the number of active particles, not the current density at each active particle.

3.3. References

1. W. C. Chueh, F. El Gabaly, J. D. Sugar, N. C. Bartelt, A. H. McDaniel, K. R. Fenton, K. R. Zavadil, T. Tylliszczak, W. Lai, and K. F. McCarty. "Intercalation Pathway in Many-Particle LiFePO_4 Electrode Revealed by Nanoscale State-of-Charge Mapping," *Nano Lett.* **13**, 866 (2013).
2. Y. Li, F. El Gabaly, T. R. Ferguson, R. B. Smith, N. C. Bartelt, J. D. Sugar, K. R. Fenton, D. A. Cogswell, A. L. D. Kilcoyne, T. Tylliszczak, M. Z. Bazant, and W. C. Chueh. "Current-induced transition from particle-by-particle to concurrent intercalation in phase-separating battery electrodes," *Nature Mater.* **13**, 1149 (2014).

4. IN-SITU LIQUID CELLS

A significant effort in this project was the development of a liquid electrochemical cell that is compatible with imaging inside a transmission electron microscope. The key requirements for the electrochemical cell include a sealed electrolyte volume that is able to contain a volatile electrolyte, a thin electron-transparent viewing region to observe electrochemical reactions in situ, and multiple electrodes to permit control and measurement of electrochemical processes. We constructed the sealed electrochemical cell using microelectromechanical systems (MEMS) processing at the MESA Fab at Sandia National Laboratories. An article describing the design and operation of the cell has been accepted for publication in the Journal of MEMS.* At the time of the writing of this report this article was not in print, so it is reproduced below.

4.1. Abstract

A standalone liquid cell for imaging and controlling electrochemical processes in a transmission electron microscope (TEM) was developed and demonstrated. The cell consisted of two silicon chips with suspended electron-transparent silicon nitride membranes that sandwiched and hermetically sealed a thin liquid layer in the TEM vacuum environment. Up to ten integrated electrodes with small exposed area allowed multiple experiments on the same chip, and the electrode geometry was designed to facilitate nanoparticle assembly or nanoscale patterning of thin film materials on the electrodes. The cell operation was demonstrated by pA-level electrochemical control and imaging of copper electrodeposition. A wide variety of materials and electrolytes are possible with the cell design, and quantitative electrochemical control at low currents was enabled by the small electrode area.

4.2. Introduction

Electrochemical processes such as electrodeposition/stripping, alloying, intercalation, and electrocatalysis often involve dramatic chemical and nanoscale structural changes in the materials involved, and the imaging and analysis possible in a transmission electron microscope (TEM) helps understand these changes as they occur. Especially for lithium ion battery materials, “open” electrochemical cells using solid-state or low-vapor-pressure ionic liquid electrolytes have given a clear window into structural changes during cycling [1], [2]. However, many standard electrochemical cells including most batteries use volatile liquid electrolytes, and the electrode behavior may be very different in the liquid environment than in the “open” cells. Specifically, phenomena such as electrode dissolution/redeposition and “solid-electrolyte interphase” (SEI) formation depend greatly on the electrolyte chosen, the product/reactant diffusion and reaction kinetics may vary with geometry and electrolyte. To image via TEM and quantitatively control nanoscale electrochemistry *in-situ* or *operando* in the native liquid environment, we have developed a set of microfabricated chips termed the TEM liquid cell “discovery platform” which is designed to be compatible with a wide variety of electrolytes and electrode materials.

The ability to image high-vapor-pressure liquid samples in an electron microscope has expanded over the last decade with reliable fabrication of suspended electron-transparent silicon nitride

(SiN_x) membranes on silicon chips that are used to sandwich a thin (100 nm to a few μm) liquid layer and isolate the liquid from the vacuum environment of the TEM [3]. Adding electrodes on one of the membranes enables electrochemical control, and following the initial designs by Ross [3]-[5], other TEM liquid electrochemical cells have been developed [6]-[9], and commercial TEM holders are available that integrate liquid flow [10] and electrodes [11], [12]. However, to date these cells have been restricted in materials flexibility with only Au, Pt, or C electrodes, difficult to align the top and bottom windows, usually fabricated with large membrane windows leading to thick liquid layers due to bowing and thus reduced imaging resolution, and limited in electrochemical control with electrode areas much larger than the viewable area and liquid layer thickness. We have sought to design a standalone, hermetically-sealed cell that features placement of active materials on Al or W current collectors before lid assembly and liquid filling, automatic alignment of the windows using alignment beads, and small-area electrodes that are exposed to the electrolyte only near the viewable area. The limited electrode area helps ensure that any changes induced electrochemically will be visible in the TEM. In addition, the electrodes are electrically well isolated to enable fA-level current measurement and control, limiting the reaction rate to technologically-relevant current densities. A variety of electrode geometries were created for work with nanoparticles, nanowires, or patterned thin films, and up to ten electrodes are present so that multiple experiments can be performed on one liquid-filled cell. Here we describe the cell design and fabrication, demonstrate examples of material placement, compare the expected electrochemical control with standard cells, and show aqueous copper electrodeposition with quantitative electrochemical control during imaging.

4.3. Liquid cell design and fabrication

The standalone liquid cell platform described here consists of two parts, a bottom chip with electrode leads and a top lid with electrolyte fill ports similar to the original design by Ross [4]. Schematic views and optical micrographs of the design are shown in Fig. 4.1.

4.3.1. Liquid Cell Design

Electron-transparent, 30-nm-thick freestanding silicon nitride films form windows at the center of both the top and bottom chips. To minimize window bowing due to the pressure differential between the liquid chamber and vacuum environment[6], [13], the nitride membranes were designed as small, 30- μm diameter circles. Since alignment of the top and bottom chips by hand within 15 μm is impractical, spherical ball lenses placed in etched pyramidal alignment holes shown in Fig. 1(f) allowed easy, automatic alignment of the SiN_x window membranes during cell assembly.

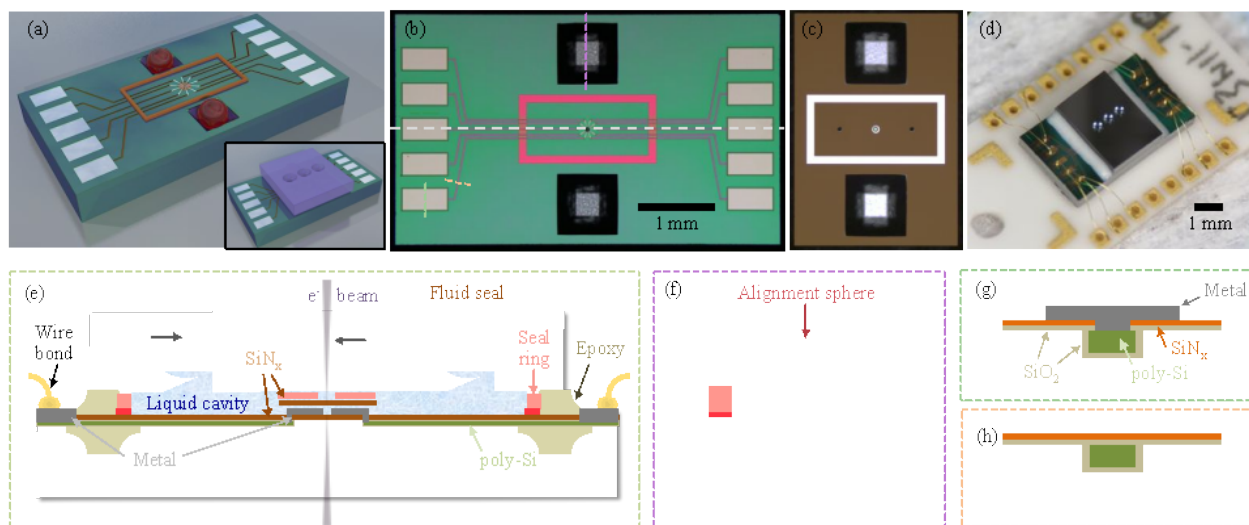


Figure 4.1. (a) Schematic render of the liquid cell showing the red alignment beads and orange seal ring with the lid included in the inset. (b) Optical micrograph of the bottom chip indicating the approximate locations of the cross-sections in (e-h) as dotted lines. (c) Optical micrograph of the underside of the top lid chip. (d) Photograph of an assembled cell wire-bonded to the TEM holder stub. (e) Schematic cross-section through the center of an assembled cell. (f-h) Cross-sectional sketches through (f) an alignment sphere including the seal ring, and the poly-Si trace with (g) and without (h) a metal bond pad showing the insulating SiO_2 and SiN_x layers.

The liquid chamber lateral boundaries and thickness were defined by a raised seal ring on both the top and bottom chips. Outside the seal ring, a 2- μm gap existed between the two chips. During assembly, the top and bottom chips were clamped together and a thin bead of epoxy was placed along the edge of the lid (seen as the white line in Fig. 1(d)). The epoxy wicked inside the 2- μm gap stopping at the seal ring (images of a disassembled cell are shown in the supplemental material, Appendix A). Inside the liquid chamber, the gap between the windows was set by a raised 100- μm -diameter mesa on the lid such that the liquid thickness was ideally 130 nm. In addition to the center view port, two liquid fill ports were also etched in the lid with a top surface diameter of 380 μm compatible with capillary tubing. The overall bottom chip dimensions were 3 mm x 5 mm, the liquid chamber was 1.68 mm x 0.78 mm, and the distance between the fill holes was 0.92 mm.

To enable controlled electrochemistry, electrical leads with minimal area exposed to the liquid were incorporated on the bottom chip. Conductive traces of doped polycrystalline silicon were buried beneath SiO_2 and SiN_x layers and isolated from the silicon chip by a SiO_2 insulator as shown in Fig. 4.1(h). At the membrane center and outer bond pads, metal electrodes were connected to the poly-Si traces with vias etched through the $\text{SiO}_2/\text{SiN}_x$ layers. The metal was either 75-nm thick Al(5% Cu) or 25 nm TiN/50 nm W chosen for both CMOS-compatible processing and electrochemical stability.

The electrode layout on the window was designed to allow assembly of nanoparticles at the tips. Ten metal electrodes converged at the window center as shown in Fig. 4.2; the tip spacing ranged from 0.25 to 1.5 μm and the smallest tip width was 0.25 μm . The geometry shown in Fig. 4.2(b-d) was chosen so that the close, sharp tips would be optimal for dielectrophoretic assembly of nanoparticles or nanowires [14]-[16] or direct placement of nanowires across electrode tips. In addition, the close spacing meant that all tips are visible in a TEM field of view.

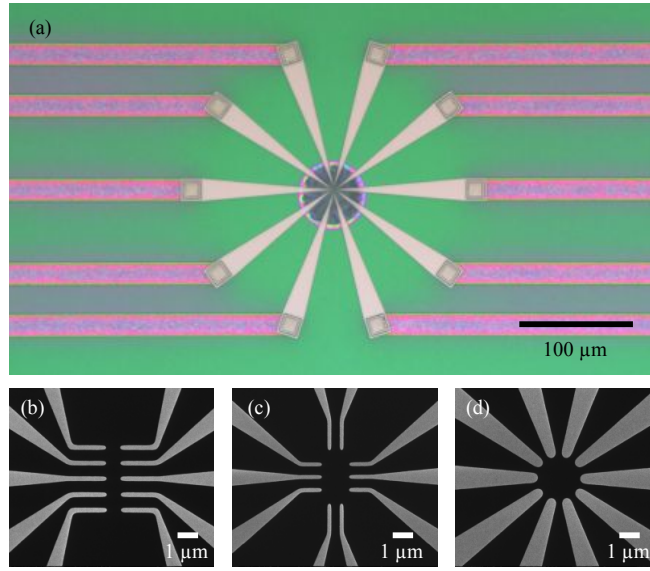


Figure 4.2. (a) Optical micrograph of the bottom chip center showing the poly-Si traces connected to W electrodes converging on the circular, suspended SiN_x membrane. (b-d) Scanning electron microscope (SEM) images showing the various electrode tip layouts.

4.3.2. Fabrication

Both the top and bottom chips are fabricated on wafer scale from double-side-polished silicon. Schematic workflows of the fabrication procedure are included in the supplemental material (Appendix A). For the bottom chip with electrodes, trenches were patterned and etched to contain the conductive traces. A thermal oxide was grown over the wafer to isolate the traces, and doped poly-Si was deposited over the entire surface. In a Damascene process the wafer was planarized such that the poly-Si remained only inside the etched traces. Another SiO_2 film was deposited to insulate the traces and subsequently serve as a Bosch etch stop. To form the lower seal ring, a 130-nm thick Si layer was deposited, patterned, and etched, and a low-stress SiN_x film was deposited over the wafer for the freestanding window. The vias for metal contact were patterned and etched through the $\text{SiO}_2/\text{SiN}_x$ layers. The metal film was then blanket deposited, patterned, and etched to define the electrodes and bond pads. To create the bead alignment holes, another SiO_2 film was deposited, patterned, and etched so that a timed anisotropic KOH etch created pyramidal wells. The view port was created by thinning the wafer to a prescribed thickness, patterning the backside and etching a tunnel with a vertical Bosch reactive ion etch process. After dicing the multiple die on each wafer, the SiN_x membrane windows were released with a HF etch to remove the oxide on both sides of the membrane.

The top lid chips were made with a similar but simpler fabrication procedure. A 2- μm thick oxide was deposited, patterned, and etched to create the upper seal ring and center mesa. A low-stress SiN_x film was deposited, and holes were patterned and etched to clear the liquid fill ports. As on the bottom chip, a deposited, patterned oxide layer served to define the KOH etch for the bead alignment holes. After thinning, the wafer backside was patterned and Bosch etched to create the liquid fill ports and center view port. The wafer was then diced and the membranes released with a HF etch.

4.4. Material placement

The liquid cell was designed as two pieces so that any material could be placed on the electrodes before sealing the lid to the bottom, and examples of post-processing to add materials to the electrode tips are shown in Fig. 4.3. Electron beam lithography and evaporation was used on the finished bottom chips to add small patches of other metals aligned to the tips; Fig. 4.3(a) shows Au tips to aid in ohmic contact to nanoparticles, while Fig. 4.3(b) shows Au squares placed on the side of electrodes to serve as inert electrodes for electrodeposition studies. To demonstrate the capability to controllably place particles of battery electrode materials, Fig. 4.3(a) shows LiFePO_4 assembled via DEP across two sets of electrode tips. For the DEP assembly, a suspension of 0.05 mg/mL LiFePO_4 in ethanol was sonicated and filtered through a 0.45 μm nylon syringe filter, and the bottom chip was placed in a bath of the suspension. An AC electric field was applied between the starred electrodes for a few minutes at 100 kHz, 8 V peak-to-peak, then the sample was rinsed in ethanol and isopropanol. The density of LiFePO_4 particles could be adjusted by changing the concentration, voltage, or duration of DEP assembly.

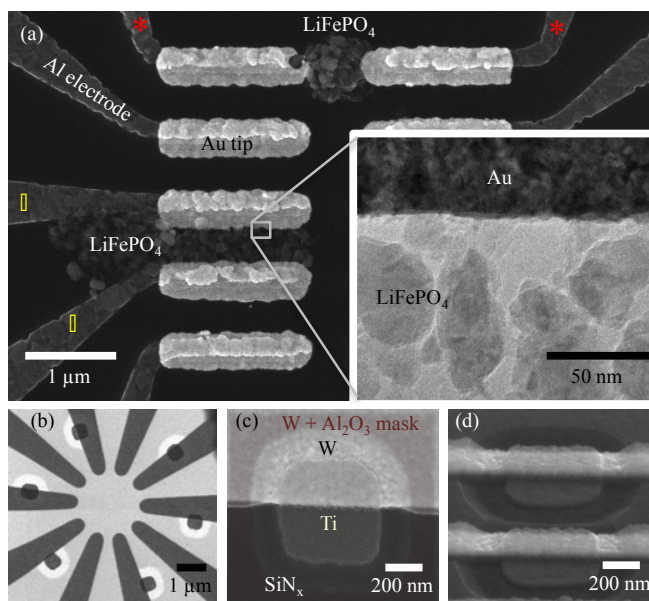


Figure 4.3. Material assembly and patterning on electrode tips. (a) SEM image of Al electrodes with Au tips patterned by electron-beam lithography and LiFePO_4 nanoparticles assembled between starred tips using DEP assembly. Inset: Brightfield STEM image of nanoparticles near Au electrode (no lid or liquid present). (b) Brightfield STEM image of Al_2O_3 -masked electrodes with Au patches patterned on the sides and bright halos where the Al_2O_3 is removed. (c) Magnified, false-colored SEM of a similar Ti patch (yellow) on the side of a W electrode masked with Al_2O_3 (red). (d) SEM image of Ti patches patterned on Al_2O_3 -masked W electrodes tilted 60°.

The electrodes could also be further masked with post-processing to insulate the metal from the liquid electrolyte if desired, as shown in Fig. 4.3(b). Though the electrodes were designed with minimal exposed metal in the liquid chamber, the exposed area of each electrode (typically 1600 μm^2) could be reduced to less than 1 μm^2 with the addition of an insulating Al_2O_3 layer followed by electron-beam lithography to remove small areas of the Al_2O_3 . A 33-nm thick layer of Al_2O_3 was conformally deposited by atomic layer deposition everywhere on the sample including over the nitride window, a 7-nm thick layer of SiO_2 was deposited by RF magnetron sputtering to improve the resist adhesion, then small areas were etched away with a wet HF-based etch through areas patterned in a polymethylmethacrylate (PMMA) resist coating. Using the same

PMMA mask, Au was deposited in the exposed areas with a liftoff procedure. A small halo is evident around the metal patches due to the wet etch undercut of the Al₂O₃ layer. Further details of the post-processing are available in the supplemental material. With the masked electrodes, any electrochemistry performed could be fully confined to the viewable window area.

After placing materials of interest on the bottom chip electrodes, the top and bottom chips were assembled and sealed in a cleanroom environment. The cell was wire-bonded to a TEM stub designed with multiple electrode leads (Nanofactory Instruments AB) as seen in Fig. 4.1(d). The chamber was filled with liquid using a micropipette to place a small droplet of liquid over one fill port, and the liquid then wicked through the chamber towards the other fill port via capillary action. Small strips of polyimide tape were placed over the fill ports, and a thin layer of epoxy was spread over the tape to form a hermetic seal; images of the filling steps are shown in the supplemental material. The liquid chamber consists of only silicon, silicon nitride, silicon dioxide, a small amount of cured epoxy, and the metal electrodes, so any electrolyte that does not attack those materials could be used including many acids and solvent-based electrolytes.

4.5. Quantitative electrochemistry considerations

The liquid cell closely mimics the environment of a standard electrochemical experiment, and similar quantitative control and interpretation of the current and voltage signals are desirable and possible in our design. Unocic recently explored the use of a commercial TEM liquid cell for quantitative electrochemistry[17] including cyclic voltammetry, chronoamperometry, and electrochemical impedance spectroscopy. While good results were obtained in most cases, the relatively large working electrodes (2860 μm^2) resulted in complete electrolysis of the electrochemically active species in the confined liquid layer and diffusion-limited reactions at the nA-level currents involved with the large electrode size. This complete electrolysis can be avoided with the smaller working electrode size at a Al₂O₃-masked electrode; e.g. the current at a 1- μm^2 working electrode with 1 mA/cm² current density is only 10 pA. By Faraday's law, the maximum current allowable to avoid reducing the concentration of the electroactive species by Δc in time t is

$$i_{\text{max}} = nF\Delta cV/t, \quad (1)$$

where n electrons are transferred per reaction, F is Faraday's constant (96485 C/mol), and V is the cell volume. In our liquid cell of volume 2.8 nL, the maximum current to avoid reducing the concentration of a 1 mM reactant by 10% in 1 hour is 7.5 pA. Hence, the small working electrode area is important not only to localize electrochemistry to the viewing window but also to avoid depletion of reactants in a typical electrochemical experiment. Note that in our design, the 28 nL fill ports will also be partially filled with electrolyte, and the diffusion time t from the fill port to the cell center is only about a minute given $t=L^2/(4D)$ with characteristic length $L\sim 500$ μm and diffusion coefficient $D\sim 10^{-5}$ cm²/s for 2-dimensional diffusion. The alternative flow cell design to refresh the electrolyte adds significant complexity to the equipment.

The small patterned electrodes are analogous to a traditional ultramicroelectrode (UME), even though the diffusion profile is radial rather than spherical due to the lid confinement. To calculate the diffusion response, the working electrode was modeled as a disc of area $A = \pi r_0^2 = 0.25$ μm^2 at the center of a cylindrically-symmetric thin cell of thickness h . The diffusion-limited steady-state current can be roughly estimated by assuming radial diffusion via Fick's second law

involving a vertical, cylindrical wire with area equivalent to A giving a wire radius $r_w = A/(2\pi h)$. Next it is assumed that liquid trapped in the fill ports fixes the concentration to the bulk value c^* at an approximate radius of $r_1 = 500 \mu\text{m}$, and the concentration at the electrode surface goes to zero. The steady-state, diffusion-limited current for this cylindrical ultramicroelectrode is then

$$i_{ss,wire} = 2\pi n F c^* D h / \ln(r_1/r_w), \quad (2)$$

where D is the diffusion coefficient. Note that eqn. 2 is equivalent to the quasi steady-state solution (where $\tau = 4Dt/r_w^2 \gg 1$) of a cylindrical UME geometry [18],

$$i_{qss,cylinder} = \frac{2\pi F A D c^*}{r_w \ln(\tau)}, \quad (3)$$

if one recognizes that at steady state, r_1^2 should replace the characteristic length $4Dt$ due to the fixed concentration at r_1 . Normalizing to the steady state current for a standard disc UME of radius r_0 ($i_{ss,UME} = 4nFDc^*r_0$) [18], the confined current is simply

$$\frac{i_{ss,wire}}{i_{ss,UME}} = \pi h / \left(2r_0 \ln \frac{2hr_1}{r_0^2} \right), \quad (4)$$

where we have approximated $r_w = r_0$. When the cell thickness becomes comparable to or greater than the electrode radius, the concentration profile is not modeled well by a simple cylindrical wire electrode, and more accurate finite-element simulations were performed using COMSOL Multiphysics software's diffusion module in a 1-D radial geometry with a flat disc electrode. Two situations were considered: (1) a simple thin cell of height h (no mesa), and (2) a confined height h out to $50 \mu\text{m}$ radius under the mesa followed by a fixed $2\text{-}\mu\text{m}$ height reservoir to most closely model our liquid cell. The results for all three models are shown in Fig. 4.4, where it is apparent that for typical TEM liquid cell thicknesses of $0.1\text{-}1 \mu\text{m}$, the steady-state currents for diffusion-limited reactions are a significant fraction of the standard ultramicroelectrode current. The mesa geometry allows somewhat larger currents. The simple analytical model is a good estimate for typical cell thicknesses below $1 \mu\text{m}$. Also included in Fig. 4.4 is the absolute current for a typical reaction, aqueous atmospheric dissolved oxygen reduction using $D = 2.5 \times 10^{-5} \text{ cm}^2/\text{s}$ and $c^* = 0.27 \text{ mM}$, and the currents are in the $10\text{-}100 \text{ pA}$ range depending on the liquid thickness.

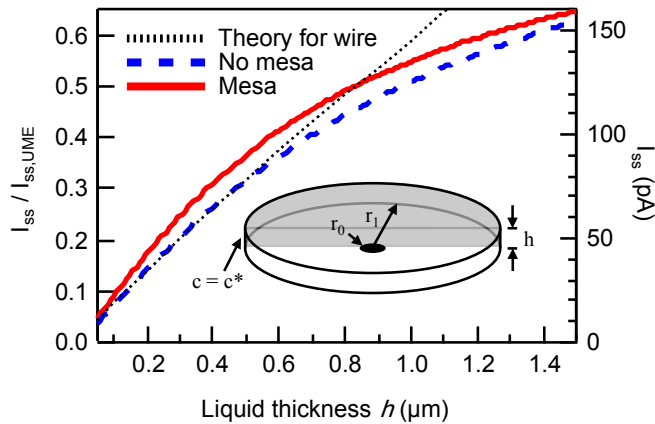


Figure 4.4. Limiting steady-state current compared to an ultramicroelectrode for a $0.25 \mu\text{m}^2$ disc electrode at the center of a $500\text{-}\mu\text{m}$ radius thin cell including the analytical theory for a cylindrical wire and simulations with and without a $50\text{-}\mu\text{m}$ radius top chip mesa (see text). Right axis shows absolute current for aqueous atmospheric dissolved oxygen reduction. Inset: sketch of geometry for calculation.

Since the small electrodes in the miniature liquid cell behave like ultramicroelectrodes, this means that the electrochemical response will be large for species at low concentration. Even though the cell volume is tiny, the electrolyte volume to electrode area ratio is much larger than

in many standard electrochemical cells such as battery coin cells. Hence, the electrochemistry will be very sensitive to low-concentration contaminants in the electrolyte such as dissolved oxygen or water in aprotic electrolytes. For example, the 10-100 pA currents demonstrated in Fig. 4.4 correspond to current densities of 4-40 mA/cm² which may be comparable to or larger than the reaction of interest (electroplating, lithiation, corrosion, etc.). On the other hand, the sensitive response means that this cell is suited for many types of analytical electrochemistry.

For fast experiments where steady state diffusion from the fill ports is not reached (experiments on the timescale of less than a minute), the cell is better modeled with thin-layer behavior in which the reactant is fully depleted in an expanding circle. The detailed response will be complicated [19]; however, the behavior again will be very similar to a UME because the quasi-steady state is very quickly reached in eqn. (3). For example, for the 0.25 μm^2 electrode size and $D=10^{-5}$ cm²/s, $\tau = 5 \times 10^4 t$ where t is in seconds, and eqn. (3) varies slowly in time when τ is large. Therefore swept-voltammetry experiments (cyclic voltammetry, linear sweep voltammetry) should appear similar to steady-state, sampled-current voltammetry experiments for typical sweep rates of order 10 mV/s even with the confined liquid cell geometry.

If the electrochemistry performed is reversible such that redox shuttling occurs between the working and counter electrodes, the close electrode spacing means that the current response may deviate [20] from the simple estimates presented so far based on diffusion from a bulk concentration in the cell, allowing higher limiting currents.

A three-electrode geometry is usually preferred, because even if the counter electrode is designed to be larger than the working electrode, current passed will polarize the counter electrode. If a third electrode is used as a pseudo reference electrode, the current drawn from it should be extremely small (a few fA) to avoid similar polarization issues. In addition, it proved useful to monitor the voltage of the counter electrode even in a three-electrode experiment to avoid large voltage excursions that could damage the counter electrode or cause bubbles to form which might push the liquid out of the imaging area.

The electron beam can also induce currents and radiolysis reactions in the liquid cell. While a detailed treatment of the beam-electrolyte interaction is beyond the scope of this paper, it should be noted that a typical TEM absolute beam current of a few nA is many orders of magnitude larger than the pA-level electrochemical currents expected. Even in the STEM imaging mode with electron dose minimized with a pA-level beam current, care should be taken to characterize the beam effects on any given system of study. A 300-keV incident electron can lose 10-100 eV in the liquid layer (calculation details are in the supplemental material), enough to induce significant chemistry and secondary electrons even though the incident electron is most likely transmitted.

4.6. Demonstration: *Operando* copper electrodeposition

The TEM liquid cell operation was tested using copper electrodeposition from aqueous copper sulfate solution. Electrochemical copper particle growth was previously imaged in the pioneering TEM liquid cell studies [4], [5], [21] on large Au electrodes, showing both the initial nucleation

density and later diffusion-controlled growth, and later beam-induced copper nanoparticle formation from solution was demonstrated [13], [22]. Under electrochemical control of an electrode much larger than the TEM field of view, the question arises of whether the imaged area is representative of the entire electrode, but our design with limited exposed electrode by masking with Al_2O_3 eliminates this uncertainty. In addition, the small, close-proximity electrodes reduce potential drops through the electrolyte and allow fast diffusion of reactants, avoiding diffusion-controlled limits to the reaction.

A bottom chip containing ten W electrodes was masked with Al_2O_3 and patterned using electron-beam lithography, and Ti/Au (10 nm/40 nm) was deposited by electron beam evaporation in small $0.25\ \mu\text{m}^2$ squares on six electrodes similar to the geometry in Fig. 3(b,c). Large $1000\text{-}\mu\text{m}^2$ Ti/Au electrodes also were deposited at the back of the remaining four electrodes to serve as counter-electrodes. After sealing the lid to the bottom chip, the cell was wire-bonded to the TEM stub, filled with an aqueous copper plating solution consisting of 0.1 M H_2SO_4 + 0.1 M CuSO_4 , and sealed. In the TEM, the zero-loss peak in EELS was not visible, so precise measurement of the liquid thickness was not possible,[13] but it was likely greater than $1\ \mu\text{m}$ due to bowing of the silicon nitride membranes.

To demonstrate the precise electrochemical control possible with this cell design, cyclic voltammetry was performed *in-situ* with the sample loaded in the TEM, shown in Fig 4.5. A copper electrode to use as a reference electrode was first deposited by applying -100 pA for 2 minutes, then the working electrode connection was switched to a nearby previously-unused electrode. Cyclic voltammetry at 20 mV/s was performed from 0.3 V to -0.2 V vs. Cu at 20 mV/s scan rate, and the third cycle is shown in Fig. 4.5(b) (the features were very similar in other cycles). In the cathodic electrodeposition direction, currents up to 200 pA are seen, and features related to Cu deposition on the Au or W peaking at -0.15 V vs. Cu as well as Cu deposition on the existing Cu at more negative potentials are seen. At positive potentials, the Cu was stripped, and the anodic current dropped abruptly at +0.06 V vs. Cu once all the copper dissolved. Also shown in Fig. 4.5 are cyclic voltammetry sweeps for a similar experiment performed in a benchtop stirred beaker cell with a $0.12\ \text{cm}^2$ electrode at 25 mV/s as well as an example of a previously published TEM liquid cell [21] with a $2000\ \mu\text{m}^2$ electrode at 25 mV/s. In both the cells with the larger electrode areas, diffusion-limited behavior is evident due to the much larger current levels, but otherwise the curve shapes are similar. Well-controlled, three-electrode, low-current electrochemistry was possible in our TEM liquid cell.

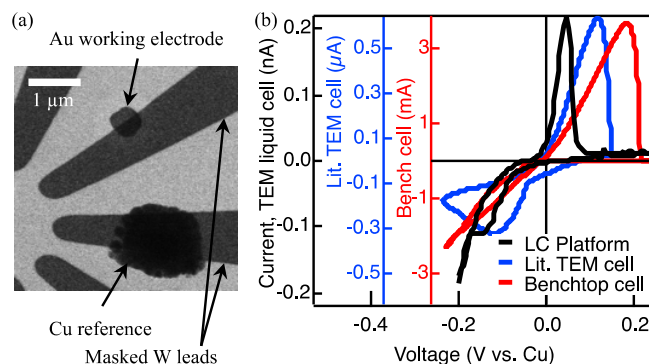


Figure 4.5. (a) BF STEM image of two electrodes in a three-electrode copper electrodeposition experiment consisting of Au patches on W leads masked with Al_2O_3 . The Cu reference was deposited in-situ. Electrolyte is present everywhere in this image; the lighter areas are imaging through both the silicon nitride membrane and electrolyte. (b) Cyclic voltammetry on the sealed cell loaded in the TEM at 20 mV/s (black trace) and data for comparison showing a simple benchtop beaker cell (red trace) and a previous TEM liquid cell [5] with larger electrode size at 25 mV/s.

Operando imaging of Cu electrodeposition was also performed in the same cell on a different electrode, and a sequence of images during linear sweep voltammetry at 5 mV/s are shown in Fig. 4.6. The images were taken in brightfield (BF) STEM mode at 300 keV with a 17 pA beam current and 5 s per frame at dose rate $60 \text{ e}^- \text{ nm}^{-2} \text{ s}^{-1}$ with the beam blanked between images. After initial nucleation of Cu grains on the small area of exposed W at -0.05 to -0.15 V vs. Cu, grains next nucleated on the Au patch, and finally the Cu grains continued to grow larger at more negative potentials. At these nA current levels no effect of the electron beam during imaging is evident in the current vs. voltage curve, but at lower current levels we noted that the electron beam could induce brief jumps of 10-50 pA in the current, so for future studies it will be critical to characterize the chemistry induced by the electron beam.

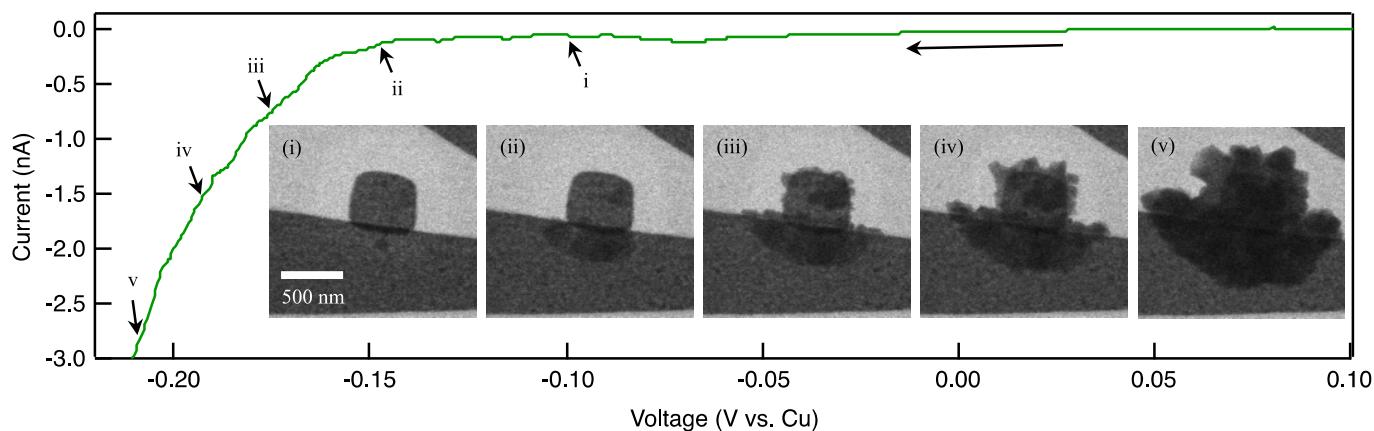


Figure 4.6. Linear sweep voltammetry of Cu electrodeposition at 5 mV/s on a masked W + Au working electrode with concurrent operando imaging. The voltages corresponding to the start of each inset image are shown by arrows.

As mentioned above, the small electrodes used here behave much like ultramicroelectrodes and as such are sensitive to contaminants in the electrolyte. This effect was evident in the Cu electrodeposition experiment, where a background current of about -60 pA had to be overcome

before Cu plating was evident in the TEM images (see the SI). The background current was likely due to dissolved oxygen reduction to form water in the acidic solution, and the current level is consistent with the calculation in Fig. 4.4. This background current also accounts for the low current efficiency of copper deposition/stripping of 51% seen in the cyclic voltammetry (Fig. 5(b)). While this liquid cell is optimized for low-current quantitative electrochemistry, care must be taken to exclude or at least understand the contaminants and side electrochemical reactions that contribute to the current especially under galvanostatic control.

4.7. Conclusion

The TEM liquid cell developed here is a versatile “discovery platform” able to work with a variety of volatile liquid electrolytes and electrode materials and is capable of precise, quantitative electrochemical control while imaging the electrode changes in the TEM. The small, sharply-tipped electrodes work well for both nanomaterial assembly by DEP and postprocessing to deposit alternative electrode materials, and the previously undemonstrated ability to insulate the bulk of the exposed metal confines the electrochemical reaction to the TEM field of view. The alignment holes/spheres greatly simplify the liquid cell assembly process compared to designs that must be aligned by hand or under a microscope. Once assembled and sealed, the liquid cell is a standalone unit, so electrochemical cycling can be done in or out of the TEM, air-sensitive materials and electrolytes can be used, and other types of optical transmission techniques may be possible.

Since electrochemical currents can be controlled to sub-pA levels on this cell, the reaction rate can be well characterized and kept to slow, relevant levels. This ability is critical if *in-situ* TEM techniques are to be compared with standard, macro-scale electrochemical experiments in which the current or voltage signatures often provide the only information about the changes in materials occurring. Linking the voltage signatures with direct images of the active area will open a new window into discrete nanoscale events in electrochemistry. At the same time, extra care should be taken to limit the effect of contaminants on these UME’s and to characterize the effects of the electron beam on both the electrodes and the electrolyte through radiolysis processes.

4.8. Acknowledgment

We thank Mike Shaw and the MESA fabrication facility for design and processing.

4.9. References

- *A. J. Leenheer, J. P. Sullivan, M. J. Shaw and C. T. Harris, “A Sealed Liquid Cell for in-situ Transmission Electron Microscopy of Controlled Electrochemical Processes,” accepted in J. MEMS (2014).
- [1] X. H. Liu, Y. Liu, A. Kushima, S. Zhang, T. Zhu, J. Li, and J. Y. Huang, “In Situ TEM Experiments of Electrochemical Lithiation and Delithiation of Individual Nanostructures,” *Adv. Energy Mater.*, vol. 2, no. 7, pp. 722–741, May 2012.

- [2] C. M. Wang, W. Xu, J. Liu, D. W. Choi, B. Arey, L. V. Saraf, J. G. Zhang, Z. G. Yang, S. Thevuthasan, D. R. Baer, and N. Salmon, "In situ transmission electron microscopy and spectroscopy studies of interfaces in Li ion batteries: Challenges and opportunities," *Microsc Microanal*, vol. 25, no. 8, pp. 1541–1547, Aug. 2010.
- [3] N. de Jonge and F. M. Ross, "Electron microscopy of specimens in liquid," *Nat Comms*, vol. 6, no. 11, pp. 695–704, Oct. 2011.
- [4] M. J. Williamson, R. M. Tromp, P. M. Vereecken, R. Hull, and F. M. Ross, "Dynamic microscopy of nanoscale cluster growth at the solid–liquid interface," *Nat Comms*, vol. 2, no. 8, pp. 532–536, Jul. 2003.
- [5] A. Radisic, P. M. Vereecken, P. C. Searson, and F. M. Ross, "The morphology and nucleation kinetics of copper islands during electrodeposition," *Surface Science*, vol. 600, no. 9, pp. 1817–1826, May 2006.
- [6] J. M. Grogan and H. H. Bau, "The Nanoaquarium: A Platform for In Situ Transmission Electron Microscopy in Liquid Media," *IEEE Trans. Electron Devices*, vol. 19, no. 4, pp. 885–894, Aug. 2010.
- [7] X. Chen, K. W. Noh, J. G. Wen, and S. J. Dillon, "In situ electrochemical wet cell transmission electron microscopy characterization of solid–liquid interactions between Ni and aqueous NiCl₂," *Acta Materialia*, vol. 60, no. 1, pp. 192–198, 2012.
- [8] E. R. White, S. B. Singer, V. Augustyn, W. A. Hubbard, M. Mecklenburg, B. Dunn, and B. C. Regan, "In Situ Transmission Electron Microscopy of Lead Dendrites and Lead Ions in Aqueous Solution," *ACS Nano*, vol. 6, no. 7, pp. 6308–6317, Jul. 2012.
- [9] Z. Zeng, W.-I. Liang, H.-G. Liao, H. L. Xin, Y.-H. Chu, and H. Zheng, "Visualization of electrode-electrolyte interfaces in LiPF₆/EC/DEC electrolyte for lithium ion batteries via in situ TEM," *Nano Lett.*, vol. 14, no. 4, pp. 1745–1750, Apr. 2014.
- [10] K. L. Klein, I. M. Anderson, and N. De Jonge, "Transmission electron microscopy with a liquid flow cell," *J Microsc*, vol. 242, no. 2, pp. 117–123, May 2011.
- [11] M. Gu, L. R. Parent, B. L. Mehdi, R. R. Unocic, M. T. McDowell, R. L. Sacci, W. Xu, J. G. Connell, P. Xu, P. Abellan, X. Chen, Y. Zhang, D. E. Perea, J. E. Evans, L. J. Lauhon, J.-G. Zhang, J. Liu, N. D. Browning, Y. Cui, I. Arslan, and C.-M. Wang, "Demonstration of an electrochemical liquid cell for operando transmission electron microscopy observation of the lithiation/delithiation behavior of Si nanowire battery anodes," *Nano Lett.*, vol. 13, no. 12, pp. 6106–6112, Dec. 2013.
- [12] M. E. Holtz, Y. Yu, D. Gunceler, J. Gao, R. Sundararaman, K. A. Schwarz, T. A. Arias, H. D. Abruña, and D. A. Muller, "Nanoscale imaging of lithium ion distribution during in situ operation of battery electrode and electrolyte," *Nano Lett.*, vol. 14, no. 3, pp. 1453–1459, Mar. 2014.
- [13] M. E. Holtz, Y. Yu, J. Gao, H. D. Abruña, and D. A. Muller, "In Situ Electron Energy-Loss Spectroscopy in Liquids," *Microsc Microanal*, vol. 19, no. 4, pp. 1027–1035, May 2013.
- [14] Y. Liu, J.-H. Chung, W. K. Liu, and R. S. Ruoff, "Dielectrophoretic Assembly of Nanowires," *J. Phys. Chem. B*, vol. 110, no. 29, pp. 14098–14106, Jul. 2006.
- [15] J. P. Sullivan, J. Huang, M. J. Shaw, A. Subramanian, N. Hudak, Y. Zhan, and J. Lou, "Understanding Li-ion battery processes at the atomic-to nano-scale," *Proc. SPIE*, vol. 7683, p. 76830B, 2010.
- [16] A. Subramanian, B. Vikramaditya, L. Dong, D. J. Bell, and B. J. Nelson, "Micro and Nanorobotic Assembly Using Dielectrophoresis," presented at the Robotics: Science

- and Systems I, Cambridge, USA, 2005.
- [17] R. R. Unocic, R. L. Sacci, G. M. Brown, G. M. Veith, N. J. Dudney, K. L. More, F. S. Walden, D. S. Gardiner, J. Damiano, and D. P. Nackashi, "Quantitative Electrochemical Measurements Using In Situ ec-S/TEM Devices," *Microsc Microanal*, pp. 1–10, Mar. 2014.
 - [18] A. J. Bard and L. R. Faulkner, *Electrochemical Methods: Fundamentals and Applications*, 2nd ed. Hoboken: John Wiley & Sons, 2001.
 - [19] A. Szabo, D. K. Cope, D. E. Tallman, P. M. Kovach, and R. M. Wightman, "Chronoamperometric current at hemicylinder and band microelectrodes: Theory and experiment," *Journal of Electroanalytical Chemistry and Interfacial Electrochemistry*, vol. 217, no. 2, pp. 417–423, Feb. 1987.
 - [20] Y. Li, W. V. Roy, L. Lagae, and P. M. Vereecken, "Effects of Counter Electrode Induced Redox Cycling on Fe(III) Reduction within Microfluidic Electrochemical Cells," *Journal of the Electrochemical Society*, vol. 161, no. 10, pp. E128–E134, Jun. 2014.
 - [21] A. Radisic, F. M. Ross, and P. C. Searson, "In Situ Study of the Growth Kinetics of Individual Island Electrodeposition of Copper," *J. Phys. Chem. B*, vol. 110, no. 15, pp. 7862–7868, Apr. 2006.
 - [22] E. A. Lewis, S. J. Haigh, T. J. A. Slater, Z. He, M. A. Kulzick, M. G. Burke, and N. J. Zaluzec, "Real-time imaging and local elemental analysis of nanostructures in liquids.," *Chem. Commun.*, May 2014.

5. ELECTROCHEMICAL MEASUREMENTS

The most standard techniques for measurement of degradation processes in Li-ion battery materials are based on pure electrochemical measurements, such as charge-discharge cycling. Numerous advancements have been made in developing new electrochemical approaches to probe degradation processes and to isolate degradation processes that occur in the anode from those that occur in the cathode. In this project, we pursued one approach which is to examine entropy changes in Li-ion electrodes as a function of the number of charge-discharge cycles. This work has been accepted for publication*, but at the time of the preparation of this report, it has not yet been published. This article is reproduced below.

5.1. Abstract

Entropy profiles of lithium cobalt oxide (LiCoO_2) electrodes were measured at various stages in the cycle life to examine performance degradation and cycling-induced changes, or lack thereof, in thermodynamics. LiCoO_2 electrodes were cycled at $C/2$ rate in half-cells (vs. lithium anodes) up to 20 cycles or $C/5$ rate in full cells (vs. MCMB anodes) up to 500 cycles. The electrodes were then subjected to entropy measurements ($\partial E/\partial T$, where E is open-circuit potential and T is temperature) in half-cells at regular intervals over the approximate range $0.5 \leq x \leq 1$ in Li_xCoO_2 . Despite significant losses in capacity upon cycling, neither cycling rate resulted in any change to the overall shape of the entropy profile relative to an uncycled electrode, indicating retention of the basic LiCoO_2 structure, lithium insertion mechanism, and thermodynamics. This confirms that cycling-induced performance degradation in LiCoO_2 electrodes is primarily caused by kinetic barriers that increase with cycling. In the case of electrodes cycled at $C/5$, there was a subtle, quantitative, and gradual change in the entropy profile in the narrow potential range of the hexagonal-to-monoclinic phase transition. The observed change is indicative of a decrease in the intralayer lithium ordering that occurs at these potentials, and it demonstrates that a cycling-induced structural disorder accompanies the kinetic degradation mechanisms.

5.2. Introduction

Lithium-ion batteries (LIB) are the most common power sources for portable electronic devices and emerging electric vehicles. Fundamental understanding of the electrode reactions and degradation mechanisms of such batteries will help lead to improvements in shelf life and operational life (also known as *cycle life*), which are necessary for the widespread commercialization of LIB-powered electric vehicles.¹ To this end, many *in situ* characterization methods² have been developed to characterize LIB electrode reactions during lithiation or delithiation, including x-ray diffraction,³ synchrotron x-ray techniques,⁴ atomic force microscopy,⁵ Raman spectroscopy,⁶ and transmission electron microscopy.⁷ Most of these methods require electrochemical cells that are specially designed and electrode materials that are nanostructured or immobilized in a particular fashion. A simple and often overlooked method of battery characterization is the electrochemical measurement of thermodynamic quantities for individual electrode reactions or full electrochemical cells.⁸ Thermodynamic studies provide fundamental insight into electrode reactions, which can lead to performance improvements, and quantitative information for thermo-electrochemical models of cells and batteries, which are

essential for predicting heat generation and preventing thermal runaway. The electrochemical measurement of thermodynamic quantities can be performed as an *in situ* diagnostic tool for cells or batteries of any form factor, including commercial cells, or as an *ex situ* evaluation of composite electrodes before or after cycling.

The three major thermodynamic quantities for an electrochemical cell are the Gibbs free energy (ΔG), entropy (ΔS), and enthalpy (ΔH). In the simplest terms, these quantities can be described as follows.⁹ The Gibbs free energy is the maximum net work (or electrical work) obtainable from the cell. The entropy is the amount of heat that is reversibly released or absorbed during the reaction. The sum of the Gibbs free energy and the entropy is the enthalpy, which amounts to the total energy in the system. These can be measured as partial molar quantities with a potentiometric method using the following equations:⁹

$$\Delta G = -nFE \quad [1]$$

$$\Delta S = nF \left(\frac{\partial E}{\partial T} \right)_P \quad [2]$$

$$\Delta H = \Delta G + T\Delta S = nF \left[T \left(\frac{\partial E}{\partial T} \right)_P - E \right] \quad [3]$$

where n is the number of electrons passed per molecule of reactant, F is the Faraday constant, E is the standard emf of the cell reaction (also referred to here as the open-circuit potential or

OCP), T is the temperature, and P is the pressure. The $\left(\frac{\partial E}{\partial T} \right)_P$ term, referred to herein simply as dE/dT , is determined by measuring the OCP of an electrochemical cell at varying temperatures. Ideally, the OCP values are measured after a period of relaxation, when the cell is as close to equilibrium as possible.

The partial molar thermodynamic quantities of lithium-ion electrode reactions are determined by testing half-cells, in which lithium metal acts as both counter and reference electrode. The ΔS term is the difference between the entropies of the positive and negative electrodes of the half-cell. The contribution from the Li/Li⁺ electrode (the negative electrode in a half-cell) is unknown but is usually assumed to be independent of both the composition of the positive electrode and the state-of-charge (SOC) of the cell.^{10, 11} Thus, the entropy values of half-cells measured using Equation 2 can be used to compare the thermodynamics of a lithium-ion electrode at varying extents of lithiation. The dependence of ΔS on the extent of lithiation of an electrode or state-of-charge of a cell is known as an *entropy profile*.⁸ Half-cells can also be used to compare the entropy profile of a pristine electrode to that of a cycled electrode that has been harvested from a full lithium-ion cell.

Entropy profiles obtained in half-cells have been reported for various LIB electrode materials, mainly Li_xTiS₂,^{10, 12-14} Li_xV₂O₅,¹⁵⁻¹⁹ LiMn₂O₄ spinel,²⁰⁻²⁵ LiCoO₂,^{11, 12, 26} and several forms of lithiated carbon.²⁶⁻³⁰ There have also been numerous reports of the entropy profiles of full lithium-ion cells,^{8, 26, 31-39} which are most useful for incorporation into thermo-electrochemical models. To the best of our knowledge, Yazami and co-workers are the only group to have examined the effect of cycling on the entropy profiles of LIBs.^{8, 35, 38} The entropy measurements from these studies were performed on full lithium-ion cells; thus, the data are useful for models that must account for changes in thermodynamics upon cycling. Such data can also be used to

establish an *in situ* state-of-health monitoring system for a particular battery composition.^{8, 38} A logical extension of this work is to examine the effect of cycling on the thermodynamics of individual electrodes rather than full cells. Thus, the changes observed in the full-cell data can be specifically and quantitatively attributed to one or both electrodes. The entropy profile of a single electrode often contains characteristics related to the insertion process (e.g. indications of intercalation, phase transition, or lithium ordering), so changes in the entropy profile at different points in the cycle life are unique and useful indications of specific degradation processes. The work presented here is a demonstration of this type of characterization on lithium cobalt oxide (LiCoO₂), the most widely used cathode material in lithium-ion batteries. As demonstrated here, the entropy profiles of LiCoO₂ electrodes that have been cycled up to 500 times reveal cycling-induced changes that have not been directly observed before, to our knowledge.

5.3. Methods

Materials. Lithium metal was purchased from Foote Mineral Corporation (USA). Lithium cobalt oxide (LiCoO₂) and mesocarbon microbeads (MCMB) were received from LiCO Technology (Japan) and Mine Safety Appliances (USA), respectively. PVDF 5130 (Solvay Plastics) and Kureha 9300 were used as binders for the cathode the anode, respectively. Denka carbon black was used as a conductive additive for both anode and cathode. LiCoO₂, MCMB, and the Denka carbon were baked out at 110°C overnight in vacuum before using. Battery-grade solvents ethylene carbonate (EC) and ethyl methyl carbonate (EMC) were purchased from Kishida Chemical Co. Ltd. (Japan) and used as received. Lithium hexafluorophosphate (LiPF₆) was purchased from Hoshimoto (Japan) and used as received.

Electrode fabrication. Slurry preparation and electrode coating were described elsewhere.⁴⁰ LiCoO₂ (cathode) slurry was coated onto aluminum foil, and MCMB (anode) slurry was coated onto copper foil. The cathode and anode compositions, respectively, were 94:3:3 wt% and 92:6:2 wt% (active material : binder : conductive additive).

Coin cell assembly. About 50 ml of EC:EMC (30:70 wt%) with 1.2 M LiPF₆ was prepared and use as a stock electrolyte solution for cells. Electrodes of 0.625-in diameter were punched from the coated foil or lithium foil. Tonen V25EKD was used as the separator for cells containing fresh electrodes, and Whatman GF/D was used as the separator for cells with cycled electrodes. Coin cells (2032-type, Hohsen) were assembled and crimped in a Hohsen automatic crimper. Half-cells (LiCoO₂ vs. lithium foil) were used for entropy measurements and for cycling experiments with 5–20 cycles, and full cells (LiCoO₂ vs. MCMB) were used for cycling experiments with 200–500 cycles. Half-cells that underwent 5–20 cycles were subjected to entropy testing within four days after cycling was completed (i.e. the same cell was used for cycling and entropy measurement in these cases). Full cells that underwent 200 or 500 cycles were disassembled after cycling using a coin cell disassembling tool (Hohsen). The cycled LiCoO₂ electrodes were then rinsed in EMC to remove residual salt and were used in new half-cells (with lithium metal counter-electrodes) for entropy measurements.

Electrochemical measurements. Galvanostatic cycling and incremental charging of coin cells was performed using an Arbin cycler (model BT-2043). Galvanostatic cycling rates are

expressed as C-rates, i.e. number of theoretical charge or discharge cycles per hour. The C-rates are based on the initial amount of LiCoO_2 on the cathode side and the theoretical capacity of 137 mAh g^{-1} , corresponding to a change from LiCoO_2 to $\text{Li}_{0.5}\text{CoO}_2$. During all electrochemical testing, coin cells were kept in a Tenney Junior temperature chamber with a Watlow F4 temperature controller. The chamber temperature was set to 30°C during cell cycling. Attached to each coin cell were battery cycler leads, voltage measurement (OCP) leads, and a J-type thermocouple on the cathode side for local temperature measurement. High-precision OCP measurement and temperature measurement were performed using an Agilent 34970A data acquisition/switch unit with two Agilent 34901A modules. Cycling and OCP/entropy measurements were each performed in triplicate, and the electrochemical data are reported as the average (markers) and standard deviation (error bars) of measurements from three replicate cells.

Measurement of entropy profiles was performed simultaneously on 20 coin cells at a time. The entropy measurement system was fully automated and integrated using the above equipment and Labview programming. Incremental cell charging was also integrated so that a full entropy profile could be automatically obtained. The entropy measurements proceeded as follows. The temperature chamber was set to constant-temperature steps at 25°C , 23°C , 24°C , 25°C , 26°C , 27°C , and 25°C with each step lasting $50 \square 60$ minutes. High-precision OCP and temperature measurements were collected simultaneously, and these data were used to calculate a single entropy value at the particular state-of-charge of the cell. Incremental charging using the Arbin cycler proceeded as follows. The cells were simultaneously charged at 30°C and C/20 rate for 30 minutes or one hour. The cells were then allowed to relax for at least 12 hours at open circuit and 30°C . The entropy measurement and incremental charging were repeated numerous times until an upper voltage limit of 4.5 V was reached during cell charging ($20 \square 30$ repeats or $16 \square 30$ days to obtain full entropy profiles on a set of 20 cells).

5.4. Results and Discussion

5.4.1. Entropy Measurement Technique and Data Analysis

Measurement of the partial molar entropy (here simply referred to as *entropy*) of lithium half-cells involved changing the temperature of each cell in steps of 1°C and measuring, with high precision, the open-circuit potential (OCP) at each temperature step. The temperature was set using a temperature chamber and controller. The temperature varied slightly throughout the chamber, so the local temperature of each cell was measured using an individual thermocouple. Because a multichannel data acquisition unit was used to measure local temperature and OCP, the entropy measurements could be performed on as many as twenty cells simultaneously. The entropy data presented here were collected over a narrow temperature range, $23 \square 27^\circ\text{C}$, so that phase transitions, thermal effects on lithium ordering, and thermal fatigue on cell components could be wholly avoided. Thus, the data presented here are focused on the thermodynamics of Li_xCoO_2 within a few degrees of room temperature. Given such a narrow temperature range and small temperature-change steps, high-precision voltage measurements are of utmost importance because of the small resultant changes in OCP.

Typical measurements of temperature over time for a single entropy measurement on a single cell are shown in Figures 5.1a and 5.1b, respectively. After a minimum of 12 hours equilibration

time, the OCP still exhibited a gradual change over time, as shown in Figure 5.1b. The non-steady OCP occurred in all cases, to varying degrees, and was presumably due to either self-discharge or the slow equilibration (via solid-state diffusion) of lithium ions in the Li_xCoO_2 lattice. Correction of the OCP data to remove the baseline drift is a common practice in electrochemical entropy measurements.^{37, 38} This ensures that the voltage changes used in calculating ΔS are purely due to temperature changes and not to a voltage drift over time. For the measurements presented here, the baseline correction and entropy calculation were performed as follows, using the data in Figure 5.1 as an example. A baseline voltage curve was determined using nine OCP data points taken at 25°C, indicated by crosses in Figure 5.1b (three data points each at the end of the first, fourth, and seventh temperature steps). The dashed line in Figure 5.1b shows a polynomial fit of these nine points. The corresponding polynomial equation was used to correct the OCP data at all temperatures, and the baseline-corrected OCP for the sample data is shown vs. time in Figure 5.1c. The result is an OCP curve with a stable baseline, and it is evident that the changes in corrected OCP are only due to changes in cell temperature. The corrected OCP values at the end of the temperature steps (circles in Figure 5.1c) were plotted vs. their corresponding temperature values (circles in Figure 5.1a), and the trend in each case was a straight line, as shown in Figure 5.1d. A least-squares linear fit of these data was performed, shown as the dashed line in Figure 5.1d. The slope of this line, in mV K^{-1} , is dE/dT , and the entropy (ΔS) was calculated using Equation 2. This same data analysis was performed for each cell at each state-of-charge. The Gibbs free energy (ΔG) was calculated using Equation 1 with the OCP value at 25°C in the middle of the entropy measurement. The enthalpy (ΔH) was calculated using Equation 3 with the same dE/dT and OCP values.

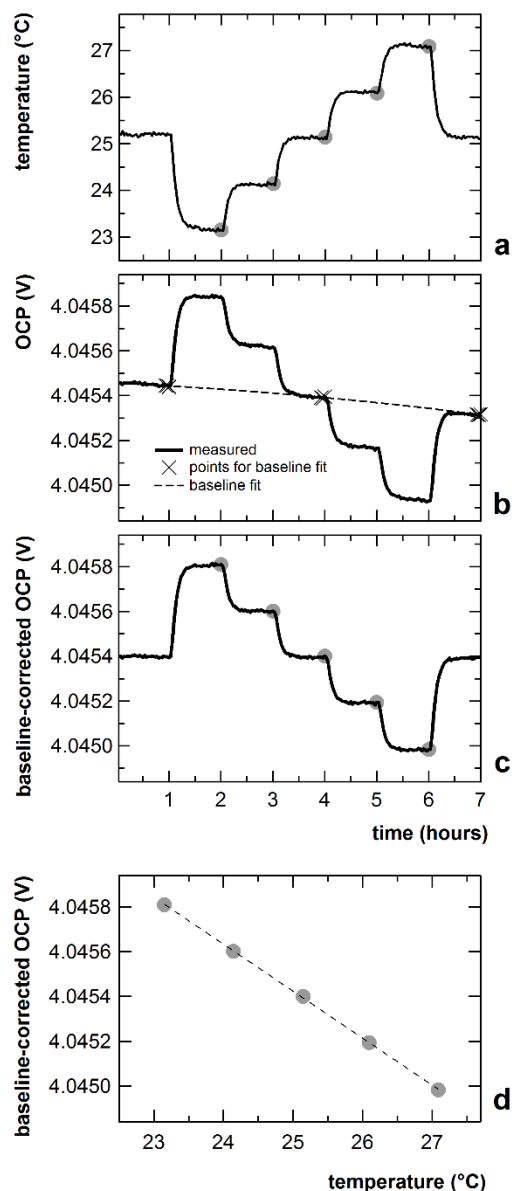


Figure 5.1. Typical data obtained for a dE/dT (entropy) measurement for a lithium-ion half-cell at a particular state-of-charge. **(a)** Temperature of the half-cell measured over time as the chamber temperature is changed in steps. **(b)** Open-circuit potential (OCP) of the half-cell measured over time. The indicated points are used to determine a baseline OCP-vs.-time curve at 25°. The baseline OCP is shown as a dashed line. **(c)** Half-cell OCP corrected, using the baseline, to have a stable voltage at 25°C. The circular markers are the points used to plot OCP vs. temperature. **(d)** Baseline-corrected OCP values from **c** plotted vs. temperature values from **a**. The dashed line is a least-squares linear fit of the data.

5.4.2. Thermodynamic Profile of Li_xCoO_2

The full thermodynamic profile (ΔG , ΔH , and $T\Delta S$) of an uncycled LiCoO_2 half-cell is shown in Figure 5.2. All data points are the average of values from three cells, and error bars are the standard deviation. The left axis in Figure 5.2b gives the *enthalpy potential*, which is the enthalpy expressed in volts (the bracketed term in Equation 3). The left axis of Figure 5.3c gives dE/dT in mV K^{-1} , and the right axis gives $T\Delta S$ in kJ mol^{-1} . The entropy profile in Figure 5.3c is very similar to others previously reported for LiCoO_2 .^{11, 26} Reynier et al. described the various regions of the Li_xCoO_2 entropy profile in terms of configurational, electronic, and vibrational (phonon) entropies.¹¹ The electronic contribution to partial molar entropy was found to be negligible compared to the total observed values. The vibrational contribution from the Li_xCoO_2 cathode was small and varied only slightly with the extent of lithiation. Thus, effects from the configurational component of entropy dominate the shape of the profile, which has been observed with other intercalation-based electrode materials such as Li_xTiS_2 ¹⁰ and $\text{Li}_x\text{Mn}_2\text{O}_4$.²²

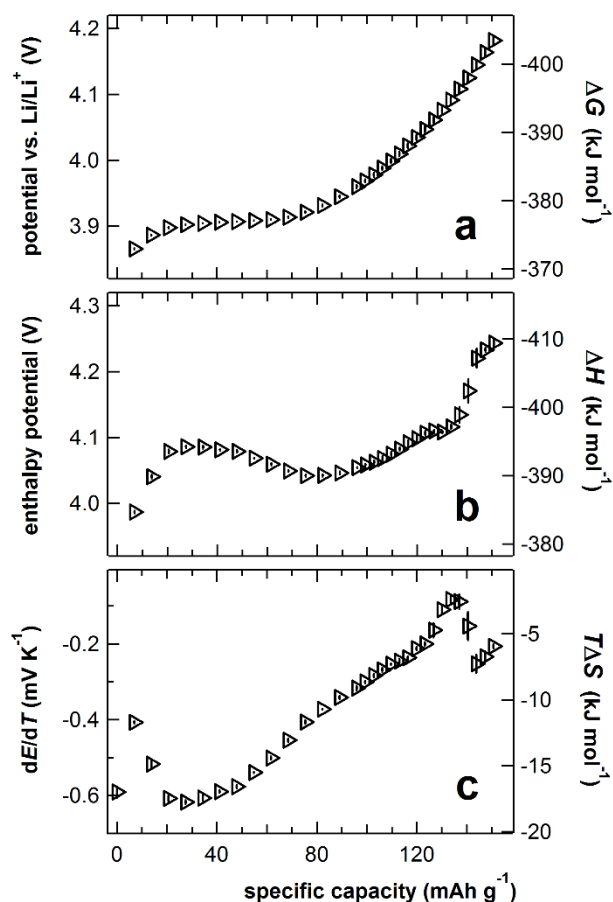


Figure 5.2. Thermodynamic quantities measured as a function of the state-of-charge of half-cells with LiCoO_2 cathodes and lithium anodes. The left-hand axes show voltage-based units, and the right-hand axes show (a) Gibbs free energy, (b) enthalpy, and (c) entropy. Each point is measured after a period of at least 12 hours of relaxation at open circuit. Markers and error bars are the average and standard deviation, respectively, of measurements from three identically prepared cells.

Reynier et al.¹¹ identified three distinct regions in the Li_xCoO_2 entropy profile and explained the shape of each in terms of configurational entropy. Each of these regions is also observed here in Figure 5.2c. From $x=0.95$ to $x=0.83$ (approximately $20 \square 50 \text{ mAh g}^{-1}$ in Figure 5.2c), the entropy profile is relatively flat and corresponds to a first-order phase transition between metallic and semiconductor phases. From $x=0.83$ to $x=0.6$ (approximately $55 \square 120 \text{ mAh g}^{-1}$ in Figure 5.2c), the monotonic increase in dE/dT follows a lattice gas model for random lithium insertion into a host lattice. From $x=0.6$ to $x=0.49$ (approximately $120 \square 150 \text{ mAh g}^{-1}$ in Figure 5.2c), Li_xCoO_2 undergoes a disordered-to-ordered phase transition accompanied by lattice distortion from hexagonal to monoclinic. This transition was first described in detail by Reimers and Dahn.⁴¹ The characteristic tilde shape in this region (a local maximum in dE/dT close to a local minimum) corresponds to a local minimum in absolute entropy, i.e. an ordered composition near $x=0.5$. The tilde shape in entropy profiles was first observed with Li_xTiS_2 and interpreted by Dahn and Haering.¹⁰ In intercalation electrode materials, this type of event occurs at certain compositions when it is energetically favorable for lithium ions in the lattice to arrange themselves in an ordered fashion rather than being randomly inserted. This type of intralayer lithium ordering is distinct from interlayer cation order, which typically exists to varying degrees in layered oxide intercalation materials like LiCoO_2 .⁴² However, an increase in interlayer disorder (also known as cation mixing) would affect intralayer lithium ordering.

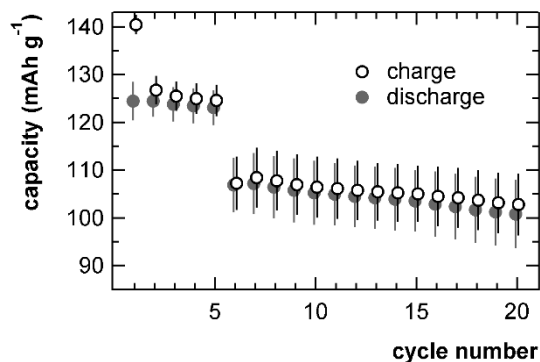


Figure 5.3. Specific (gravimetric) capacity of galvanostatically cycled half-cells containing LiCoO_2 cathodes and lithium anodes. Cycling rate was C/5 (charge) and C/2 (discharge) for the first five cycles and C/2 (charge and discharge) thereafter. Markers and error bars are the average and standard deviation, respectively, of measurements from three identically prepared cells.

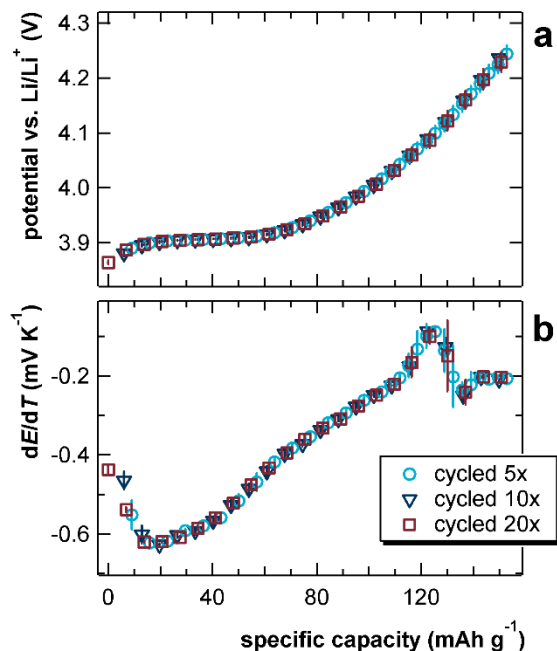


Figure 5.4. (a) Open-circuit potential and (b) dE/dT of half-cells containing LiCoO_2 cathodes and lithium anodes after cycling according to the conditions in Figure 5.3 (C/2 rate). Markers and error bars are the average and standard deviation, respectively, of measurements from three identically prepared cells.

The thermodynamic quantities in Figure 5.2 and subsequent plots are given as a function of specific gravimetric capacity instead of x in Li_xCoO_2 . This is because the first delithiation of LiCoO_2 contains a significant amount of irreversible capacity from the electro-oxidative decomposition of electrolyte species, which makes it difficult to determine the exact value of x at a given nominal capacity. However, the entropy data in Figure 5.2c can be superimposed upon and match up closely with those of Reynier et al.¹¹ and Thomas and Newman.²⁶ The only quantitative difference is in the order-disorder transition region, where the tilde shapes from the two other studies are more pronounced, to differing degrees, than that in the present work. In other words, the difference between the local maximum and minimum is significantly lower in the present work. This difference can be explained by the difference in either the average temperature of entropy measurement or the source of LiCoO_2 powder used. In an entropy study on LiCoO_2 -graphite cells, Takano et al. reported that temperature of entropy measurement and the manufacturer of the cells both affected the pronouncement of the tilde at $x=0.5$.⁴³ Presumably, the cell manufacturers used different sources of LiCoO_2 powder, and differences in particle size distribution or impurities among powder samples could explain the quantitative difference in ordering behavior. Another explanation would be that there are differences in the initial interlayer cation ordering. This type of ordering is sensitive to synthesis conditions, and LiCoO_2 from some sources may be slightly disordered. The presence of transition metals on the “lithium layer” (the 3a octahedral sites in the $\text{R}\bar{3}\text{m}$ structure) would certainly disrupt the intralayer lithium ordering and result in a less pronounced tilde in the entropy profile.

5.4.3. Effect of Fast Cycling

The goal of the present study is to examine the effect of cycling on the delithiation entropy profile of LiCoO_2 . Cycling at two different rates, $C/2$ (“fast”) and $C/5$ (“slow”), was performed, and the entropy profiles of the cycled electrodes in half-cells were subsequently measured. Cycling results (capacity vs. cycle number) for half-cells cycled at $C/2$ (the “fast” rate) are shown in Figure 5.3. The first five cycles are formation cycles, in which the charging rate was $C/5$ and the discharge rate was $C/2$. Only a small number of cycles were studied at this fast rate, so the cycling was performed in half-cells without concern for lithium dendrite formation at the anode. As shown in Figure 5.3, cycling capacity after 20 cycles was 20% lower than the initial discharge capacity. This is a significant amount of cycling-induced degradation. The loss in capacity is wholly attributable to the LiCoO_2 electrode because the molar amount of lithium at the lithium metal electrode was in great excess of that at the LiCoO_2 electrode. Any lithium lost to side reactions at the cathode (electrolyte decomposition and electrochemical formation of passivating surface layers) would be readily replenished upon discharge with lithium from the anode. Thus, the loss in capacity at the LiCoO_2 cathode was due to changes in the composite electrode or the LiCoO_2 itself and not simply to a depletion of electroactive lithium in the cell.

The OCP and entropy (as dE/dT in mV K^{-1}) of LiCoO_2 electrodes after cycling at $C/2$ rate are shown in Figure 5.4. The shape and magnitude of both curves were retained after cycling 5, 10, and 20 times. There were no discernible changes to the thermodynamic quantities after cycling at $C/2$ up to 20 cycles despite the loss in cycling capacity. The full $\sim 140 \text{ mAh g}^{-1}$ capacity was recovered during these thermodynamics measurements because the cells were charged at such a slow rate (one-hour charging steps at $C/20$ with open-circuit rest periods of 20-24 hours between steps, for an effective rate of $\sim C/500$). Retention of the shape of the entropy profile after cycling proves that the intercalation mechanism as described above remains the same after the degradation in performance caused by 20 cycles at $C/2$. The observation that OCP (when measured with slow, incremental charging) does not change with cycling is in qualitative agreement with a thermodynamics study of full lithium-ion cells (LiCoO_2 vs. graphite) after cycling at $C/2$.³⁵ In that case, there were only minor changes in full cell OCP after 1000 cycles at $C/2$ despite $\sim 30\%$ losses in cycling capacity.

These results suggest that the loss in cycling capacity at $C/2$ is purely due to kinetic effects and not to a fundamental change in the thermodynamics or structure of LiCoO_2 . Examples of kinetic degradation effects are the continued growth of the passivating layer on the cathode (which would cause increasing ohmic and transport barriers) and particle breaking or cracking (which would increase ohmic resistance and create electrochemically inaccessible regions of LiCoO_2). Evidence for growth of the passivating layer was previously observed in LiCoO_2 electrodes that had been cycled at $C/2$ ⁴⁴ rate or $1C$ rate⁴⁵ in commercial lithium-ion cells. Those studies showed that the “surface resistance” at the cathode, measured with electrochemical impedance spectroscopy, increased with increased cycling. Furthermore, Aurbach et al. concluded that capacity loss in LiCoO_2 electrodes resulting from cycling or storage was due to surface phenomena and not structural changes.⁴⁶ The effect of particle cracking or breaking was previously observed using transmission electron microscopy (TEM) on LiCoO_2 particles that had been cycled 50 times at $C/5$ rate⁴⁷ or 286 times at $1C$ rate.⁴⁸ Thus, the previous reports and the

results reported here are all in agreement that kinetic degradation effects are a significant contributor to cycling-induced performance losses in cells with LiCoO_2 cathodes.

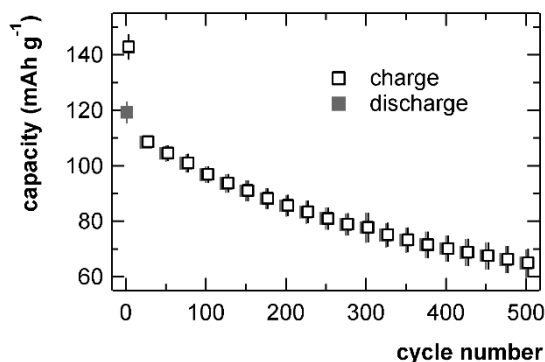


Figure 5.5. Specific (gravimetric) capacity of galvanostatically cycled cells containing LiCoO_2 cathodes and MCMB anodes. Cycling rate was C/10 (charge) and C/5 (discharge) for the first five cycles and C/5 (charge and discharge) thereafter. Markers and error bars are the average and standard deviation, respectively, of measurements from three identically prepared cells.

5.4.4. Effect of Slow Cycling

For longer-term cycling experiments, a slower rate of C/5 (relative to LiCoO_2) was used. Capacity data for full cells (LiCoO_2 vs. MCMB) cycled at C/5 (the “slow” rate) are shown in Figure 5.5. The first five cycles are formation cycles, in which the charging rate was C/10 and the discharge rate was C/5. The use of full cells is a closer representation of commercial, rechargeable, lithium-ion batteries and allows high amounts of cycling without concern for dendrite formation. As shown in Figure 5.5, cycling capacity after 500 cycles was 46% lower than the initial discharge capacity. The loss in capacity in these full cells is not readily attributable to either the LiCoO_2 electrode or the MCMB electrode because the capacities of both electrodes were roughly matched. Any lithium consumed in side reactions (electrolyte decomposition and electrochemical formation of passivating surface layers) would be irreversibly lost and at least partially responsible for the loss in cycling capacity. Studies of commercial LIB cells previously demonstrated that the LiCoO_2 cathode was largely responsible for voltage fade, and the graphitic anode was largely responsible for capacity fade. However, both electrodes experienced both types of performance degradation to some extent.^{45, 46}

After cycling at C/5 to the designated number of cycles (5, 200, or 500), the full cells were disassembled. The cycled LiCoO_2 electrodes were rinsed in EMC and transferred to half-cells with new lithium counter-electrodes for entropy measurements. The OCP and entropy (as dE/dT) of these LiCoO_2 electrodes after cycling are shown in Figure 5.6. The OCP and entropy profiles of electrodes that were cycled five times (Figure 5.6) match those of uncycled electrodes (Figure 5.2) very closely. As shown in Figure 5.6, electrodes that were cycled 200 and 500 times lost a significant amount of capacity. They did not reach the 140 mAh g^{-1} full capacity even at this low effective rate of $\sim\text{C}/500$. This suggests that a significant amount of the loss in cycling capacity of the full cells was due to degradation of the LiCoO_2 cathode. Some of the capacity loss could also be due to a slight loss of material in transferring the electrode from a spent, full cell to a new half-cell. Regardless of the latter possibility, LiCoO_2 electrodes that were cycled 500 times at C/5 and re-assembled into new half-cells had severe rate limitations. This suggests

that the kinetic effects discussed above (surface resistance and particle cracking) were also a significant contributor to the performance losses of LiCoO_2 electrodes cycled at the slower rate of C/5.

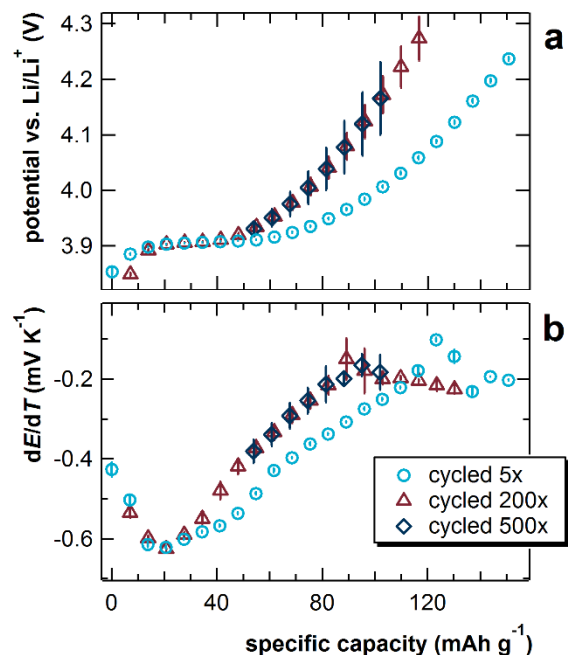


Figure 5.6. (a) Open-circuit potential and (b) dE/dT of half-cells containing LiCoO_2 cathodes and lithium anodes. The LiCoO_2 electrodes were cycled in full cells (vs. MCMB) according to the conditions in Figure 5.5 (C/5 rate), removed from the full cells, and then placed in new half-cells for the measurements in a and b. Markers and error bars are the average and standard deviation, respectively, of measurements from three identically prepared cells.

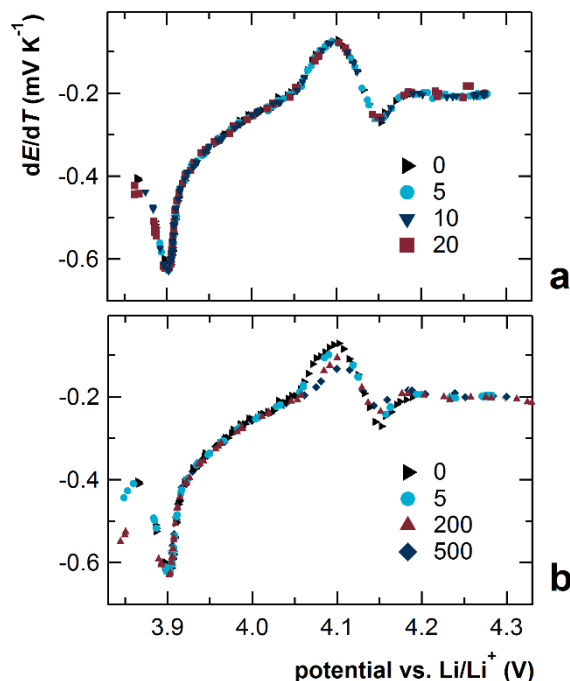


Figure 5.7. Thermodynamic data for LiCoO_2 from Figures 5.4 and 5.6 expressed as dE/dT vs. OCP (entropy vs. Gibbs free energy). The LiCoO_2 electrodes were cycled at (a) the “fast” rate of C/2 and (b) the “slow” rate of C/5, and the number of cycles is shown in the legends. All of the data points from three identically prepared cells for each condition (cycling rate and number of cycles) are shown individually.

The OCP profiles and entropy profiles of LiCoO_2 electrodes that were cycled 200 and 500 times appear to have retained the same general shape as those of uncycled electrodes. However, the loss in capacity with cycling resulted in a loss of resolution in the OCP curves and entropy profiles, as shown in Figure 5.6. Furthermore, the samples that experienced high amounts of cycling exhibited larger amounts of error. These factors make it difficult to determine whether there were any real changes in the thermodynamic quantities of LiCoO_2 after cycling or whether the observed changes were primarily due to a loss in capacity. A clearer way to examine the thermodynamic data is to plot entropy versus the OCP (or proportionally, ΔG) as demonstrated by Yazami and Maher.^{8,35} The two dependent variables have a unique relationship because OCP changes monotonically with the independent variable, gravimetric capacity. Thus, any changes in the thermodynamics can be observed clearly and independently of changes in total capacity. Furthermore, each replicate data point can be plotted separately (as entropy vs. OCP for an individual sample cell) rather than plotting averages of replicate samples. This results in higher-

resolution data as the slight OCP variations among repeat samples result in a more continuous entropy curve. Both fast-rate and slow-rate data are presented in this manner in the following section.

5.4.5. Cycling-Induced Changes in Entropy

Entropy profiles of uncycled and cycled LiCoO_2 electrodes are plotted in Figures 5.7 and 5.8 as dE/dT vs. OCP. As shown in Figure 5.7(a), it is clear that the entropy profiles after zero, 5, 10, and 20 cycles at the fast rate completely overlap one another in each portion of the curve. There are no measureable differences among the entropy profiles even though there was significant loss in cycling capacity. Figure 5.8(a) shows a more detailed view of the tilde-shaped portion of the curve, in which the most complicated entropy-OCP dependence exists. It is possible that there is a slight increase in dE/dT at the local minimum (at 4.15 V vs. Li/Li^+) after 20 cycles. It is impossible with the given amount of data to discern whether this change is statistically significant and whether it gradually occurs during the first 20 cycles. Similarly, Maher and Yazami observed slight changes in this portion of the entropy after cycling at $C/2$, but there was no clear trend and no indication of statistical significance.³⁵ Furthermore, the entropy data of Maher and Yazami were measured with full lithium-ion cells, in which the graphite anode may give a non-negligible contribution to entropy. This complication makes it unclear whether the changes observed with cycling were due to the cathode, anode, or both. Conversely, the data presented here in Figure 5.7(a) and 5.8(a) show that there are no significant changes in the entropy profile of LiCoO_2 after 20 cycles at $C/2$ and 20% loss in cycling capacity.

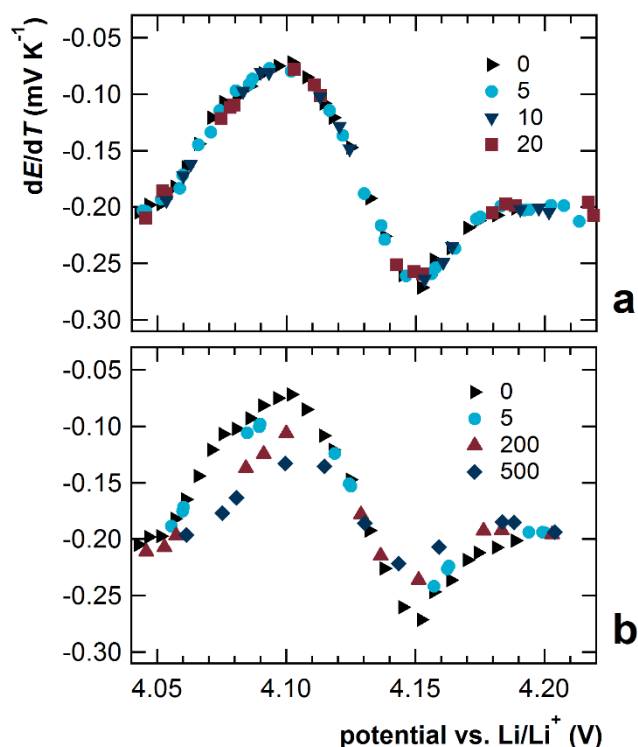


Figure 5.8. Detail of the LiCoO_2 thermodynamic data from Figure 5.7 with focus on the tilde-shaped portion of the curve, where the disordered-to-ordered and hexagonal-to-monoclinic phase transition occurs.

The entropy vs. OCP of LiCoO_2 electrodes after cycling at the slow rate in full cells is shown in Figures 5.7(b) and 5.8(b). After 500 cycles and 46% capacity loss, the shape and characteristic regions of the entire entropy profile remained unchanged, as shown in Figure 5.7(b). This proves

that the lithium-insertion mechanism as described above remained the same despite significant performance degradation. Furthermore, there were no quantitative changes to the entropy profile in the OCP range 3.90–4.05 V vs. Li/Li⁺. Thus, the two lithiation mechanisms that are active in this range (the metallic-to-semiconductor phase transition and lattice gas-type disordered intercalation) operated identically in degraded electrodes to at least 500 cycles as they did in uncycled electrodes. However, with increased cycling, there was a quantitative and gradual change in the tilde-shaped portion of the entropy curve (greater than 4.05 V vs. Li/Li⁺), as shown in detail in Figure 5.8(b). This part of the curve corresponds to the hexagonal-to-monoclinic lattice distortion accompanied by intralayer ordering of the intercalated lithium. As the amount of cycling increased, the local maximum dE/dT value (at 4.10 V) decreased and the local minimum (at 4.15 V) increased; thus, the local minimum in absolute entropy increased. Because the distinctive tilde shape in dE/dT curves arises solely from configurational entropy,¹⁰ the observed change indicates that the intercalated lithium became gradually less ordered with increasing amounts of cycling.

The cycling-induced change in the tilde-shaped portion of the dE/dT curve of Figure 5.8(b) is a subtle one. As discussed above, this portion of the entropy profile quantitatively differs among various studies^{11, 26, 43} and among various LiCoO₂ samples within the same study⁴³ even though the LiCoO₂ structure is always the same. The variations in the tilde shape among these different studies were more quantitatively significant than the cycling-induced changes observed here despite the fact that all the LiCoO₂ electrodes in question exhibited comparable initial performance. Thus, the subtle change in thermodynamics observed here cannot be responsible for the large loss in cycling capacity. As with the C/2-cycled samples discussed above and LiCoO₂ electrodes from previous reports,^{44–48} kinetic factors are the most significant contributor to performance degradation in the C/5-cycled electrodes studied here.

Despite the dominance of kinetic factors in the degradation of the electrodes studied here, the change in thermodynamics observed in the C/5-cycled cells reveals a fundamental, cycling-induced change in the LiCoO₂ itself. The decrease in intralayer lithium ordering observed here may due to a change in particle size, particle shape, or LiCoO₂ purity, or it may be indirect evidence of increased interlayer cation mixing. Cycling-induced cation mixing (i.e. disorder) was previously observed using TEM and electron diffraction analysis on LiCoO₂ particles.^{45, 47} Attempts at observing cation mixing on a more global scale using X-ray diffraction (XRD) analysis have produced mixed results. Various researchers observed an increase,⁴⁵ decrease,⁴⁹ or lack of change^{46, 48} in the peak intensity ratio I_{003}/I_{104} with cycling. This intensity ratio is theoretically correlated to cation mixing for an XRD sample with no preferred crystallite orientation.⁴⁷ It is unknown whether the I_{003}/I_{104} values in these reports were truly an unbiased measure of cation mixing or whether they were significantly influenced by preferred orientation. By contrast, the results presented here, using entropy profiles, provide unambiguous evidence of a gradual, repeatable, and cycling-induced disorder measured globally on LiCoO₂ electrode samples.

5.5. Conclusion

The measurement of thermodynamic quantities and entropy profiles is a useful way to probe degradation processes in electrodes for lithium-ion batteries. This concept is demonstrated herein using lithium cobalt oxide as an active electrode material that has already been well-characterized with various other methods. The data reported here show subtle thermodynamic changes in LiCoO_2 after cycling while confirming previous reports that the performance losses caused by cycling are largely due to kinetic factors such as growth of the passivating surface layer and formation of cracks in LiCoO_2 particles.

Half-cells with LiCoO_2 cathodes were cycled at $C/2$ for small numbers of cycles and then subjected to entropy measurements. Entropy measurements were performed by allowing the cell to relax at open circuit and then measuring the changes in OCP after applying small changes in temperature. The slope of the OCP-temperature curve, or dE/dT , is proportional to the partial molar entropy of the electrode reaction at that particular state-of-charge (or extent of lithiation). The procedure was repeated at varying states of charge so that an entire entropy profile of the electrode could be obtained. LiCoO_2 electrodes that were cycled 20 times at $C/2$ in half-cells experienced significant loss in specific capacity but showed no measureable changes in the entropy profile. This shows that the degradation in performance was caused by increasing kinetic barriers to lithiation and delithiation of Li_xCoO_2 rather than a change in the structure or thermodynamics of the material itself.

Full cells with LiCoO_2 cathodes and MCMB anodes were cycled at $C/5$ for hundreds of cycles (up to 500). After a given amount of cycling the LiCoO_2 electrodes were transferred to new half-cells for entropy measurements. While these cells exhibited up to 46% loss of cycling capacity, the LiCoO_2 electrodes experienced only subtle changes in entropy. Thus, the electrodes cycled at $C/5$ also experienced performance losses that were dominated by kinetic effects. The intercalation mechanism remained unchanged, evidenced by the retention of the entropy profile shape. The unique dependence between entropy (proportional to dE/dT) and Gibbs free energy (proportional to OCP), which is independent of electrode capacity, experienced only small quantitative changes, but they are fundamentally important. The small, gradual change in thermodynamics that was observed occurred at a state-of charge at which Li_xCoO_2 undergoes a disordered-to-ordered phase transition. The change in the entropy profile showed that the arrangement of lithium ions during this transition becomes gradually less ordered as the electrode is cycled more. This decrease in ordering may be the result of an increase in interlayer cation mixing, which has been observed previously but only with localized characterization of LiCoO_2 particles. The method presented here unambiguously shows a cycling-induced disorder in LiCoO_2 , observed globally on the entire electrode sample, which occurs even when the kinetic barriers to cycling performance are dominant. This also demonstrates that entropy measurements can be effectively used to reveal underlying degradation mechanisms and structural changes in lithium-ion electrodes.

5.6. Acknowledgements

The authors thank John Sullivan and Mark Rodriguez, both of Sandia National Laboratories, for helpful discussions.

5.7. References

- *N. S. Hudak, L. E. Davis, and G. Nagasubramanian, "Cycling-Induced Changes in the Entropy Profiles of Lithium Cobalt Oxide Electrodes," accepted for publication in *J. Electrochem. Soc.* (2014).
1. A. Barré, B. Deguilhem, S. Grolleau, M. Gérard, F. Suard and D. Riu, *J Power Sources*, **241**, 680 (2013).
 2. S. F. Amalraj and D. Aurbach, *J Solid State Electr*, **15**, 877 (2011).
 3. J. R. Dahn and R. R. Haering, *Can J Phys*, **60**, 307 (1982).
 4. J. McBreen, *J Solid State Electr*, **13**, 1051 (2009).
 5. L. Y. Beaulieu, V. K. Cumyn, K. W. Eberman, L. J. Krause and J. R. Dahn, *Review of Scientific Instruments*, **72**, 3313 (2001).
 6. T. Itoh, K. Abe, M. Mohamedi, M. Nishizawa and I. Uchida, *J Solid State Electr*, **5**, 328 (2001).
 7. X. H. Liu, Y. Liu, A. Kushima, S. Zhang, T. Zhu, J. Li and J. Y. Huang, *Adv Energy Mat*, **2**, 722 (2012).
 8. R. Yazami and K. Maher, in *Lithium-Ion Batteries: Advances and Applications*, ed. G. Pistoia, p. 567, Elsevier, Amsterdam (2014).
 9. A. J. Bard and L. R. Faulkner, *Electrochemical methods : fundamentals and applications*, p. xxi, Wiley, New York (2001).
 10. J. R. Dahn and R. R. Haering, *Can J Phys*, **61**, 1093 (1983).
 11. Y. Reynier, J. Graetz, T. Swan-Wood, P. Rez, R. Yazami and B. Fultz, *Phys Rev B*, **70**, 174304 (2004).
 12. A. Honders, J. M. der Kinderen, A. H. van Heeren, J. H. W. de Wit and G. H. J. Broers, *Solid State Ionics*, **14**, 205 (1984).
 13. D. H. Shen, S. Surampudi, G. Halpert and K. M. Abraham, in *New Sealed Rechargeable Batteries and Supercapacitors*, ed. B. M. B. e. al., p. 367, The Electrochemical Society Proceedings Series, Pennington, NJ (1993).
 14. A. H. Thompson, *Physica B+C*, **105**, 461 (1981).
 15. S. Bach, J. P. Pereira-Ramos, N. Baffier and R. Messina, *J Electrochem Soc*, **137**, 1042 (1990).
 16. R. Baddour, J. P. Pereira-Ramos, R. Messina and J. Perichon, *J Electroanal Chem*, **314**, 81 (1991).
 17. J. P. Pereira-Ramos, R. Messina, C. Piolet and J. Devynck, *Electrochim Acta*, **33**, 1003 (1988).
 18. A. V. Popov, Y. G. Metlin and Y. D. Tretyakov, *J Solid State Chem*, **32**, 343 (1980).
 19. Y. D. Tretyakov, A. V. Popov and Y. G. Metlin, *Solid State Ionics*, **17**, 265 (1985).
 20. S. Bach, J. P. Pereira-Ramos, N. Baffier and R. Messina, *Electrochim Acta*, **37**, 1301 (1992).
 21. S.-W. Kim and S.-I. Pyun, *Electrochim Acta*, **46**, 987 (2001).
 22. Y. Kobayashi, Y. Mita, S. Seki, Y. Ohno, H. Miyashiro, M. Nakayama and M. Wakihara, *J Electrochem Soc*, **155**, A14 (2008).
 23. K. E. Thomas, C. Bogatu and J. Newman, *J Electrochem Soc*, **148**, A570 (2001).
 24. W. C. Wong and J. Newman, *J Electrochem Soc*, **149**, A493 (2002).

25. R. Yazami, Y. Reynier and B. Fultz, *ECS Transactions*, **1**, 87 (2006).
26. K. E. Thomas and J. Newman, *J Power Sources*, **119-121**, 844 (2003).
27. J. Gong and H. Wu, *Electrochim Acta*, **45**, 1753 (2000).
28. Y. Reynier, R. Yazami and B. Fultz, *J Power Sources*, **119-121**, 850 (2003).
29. Y. F. Reynier, R. Yazami and B. Fultz, *J Electrochem Soc*, **151**, A422 (2004).
30. R. Yazami and Y. Reynier, *J Power Sources*, **153**, 312 (2006).
31. S. Al Hallaj, J. Prakash and J. R. Selman, *J Power Sources*, **87**, 186 (2000).
32. S. Al Hallaj, R. Venkatachalapathy, J. Prakash and J. R. Selman, *J Electrochem Soc*, **147**, 2432 (2000).
33. K. Jalkanen, T. Aho and K. Vuorilehto, *J Power Sources*, **243**, 354 (2013).
34. K. Maher and R. Yazami, *Electrochim Acta*, **101**, 71 (2013).
35. K. Maher and R. Yazami, *J Power Sources*, **247**, 527 (2014).
36. K. Onda, H. Kameyama, T. Hanamoto and K. Ito, *J Electrochem Soc*, **150**, A285 (2003).
37. V. V. Viswanathan, D. Choi, D. Wang, W. Xu, S. Towne, R. E. Williford, J.-G. Zhang, J. Liu and Z. Yang, *J Power Sources*, **195**, 3720 (2010).
38. R. Yazami, J. McMenemy, Y. Reynier and B. T. Fultz, Battery State of Health Assessment System, in, USPTO Editor (2010).
39. A. Eddahech, O. Briat and J.-M. Vinassa, *Energy*, **61**, 432 (2013).
40. G. Nagasubramanian, *Int. J. Electrochem. Sci.*, **2**, 913 (2007).
41. J. N. Reimers and J. R. Dahn, *J Electrochem Soc*, **139**, 2091 (1992).
42. M. S. Whittingham, *Chem Rev*, **104**, 4271 (2004).
43. K. Takano, Y. Saito, K. Kanari, K. Nozaki, K. Kato, A. Negishi and T. Kato, *J Appl Electrochem*, **32**, 251 (2002).
44. D. Zhang, B. S. Haran, A. Durairajan, R. E. White, Y. Podrazhansky and B. N. Popov, *J Power Sources*, **91**, 122 (2000).
45. P. L. Moss, G. Au, E. J. Plichta and J. P. Zheng, *J Electrochem Soc*, **157**, A1 (2010).
46. D. Aurbach, B. Markovsky, A. Rodkin, E. Levi, Y. S. Cohen, H. J. Kim and M. Schmidt, *Electrochim Acta*, **47**, 4291 (2002).
47. H. Wang, Y. I. Jang, B. Huang, D. R. Sadoway and Y. M. Chiang, *J Electrochem Soc*, **146**, 473 (1999).
48. J. Li, E. Murphy, J. Winnick and P. A. Kohl, *J Power Sources*, **102**, 294 (2001).
49. J. Zhou and P. H. L. Notten, *J Power Sources*, **177**, 553 (2008).

6. THEORY AND MODELING

Many of the degradation mechanisms in Li-ion batteries are especially difficult to model – at least from first principles – as they often involve interfaces between solid and liquid phases as well as the transport of ions and electrons. In this project, we focused the theory and modeling on degradation mechanisms associated with reduction or oxidation across the solid/liquid electrochemical interface. One of the primary degradation mechanisms is the reduction of the battery electrolyte – typically a solvent based on ethylene carbonate – at the battery anode and the formation of a solid product layer of reduction products, known as the solid-electrolyte-interphase (SEI). Two significant publications resulted from this work (summarized below).

6.1. First principles investigation of the reduction of ethylene carbonate

Different electrochemical pathways have been proposed for the reduction of ethylene carbonate at Li-based anodes: a one-electron process and a two-electron process. In the absence of first principles simulation, it was assumed that the one-electron process always dominates, and this results in a predictable sequence of reduction products. However, we have examined this reduction process using ab initio quantum chemistry calculations, and we found that a two-electron reduction process can dominate in certain stages of the formation of the SEI layer.[1] The electrochemical conditions over which the two-electron process dominates can be summarized in the form of a “phase diagram”, as shown in Figure 6.1.

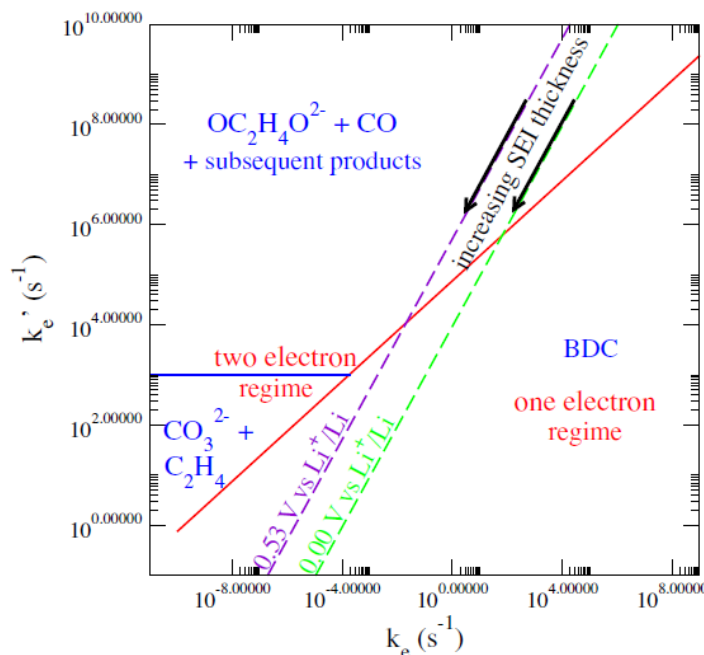


Figure 6.1. Different SEI formation regimes, assuming steady state reactions and a homogeneous reaction zone. The x- and y-axes are the 1-electron and 2-electron tunneling rates. Green and violet dashed lines represent applied potentials of 0.0 and 0.53 V versus Li^+/Li (s). $\text{OC}_2\text{H}_4\text{O}_2^-$ is not the final product. Oligomers are not explicitly considered but are secondary products in the $\text{OC}_2\text{H}_4\text{O}_2^-$ region and may be present at low k_e rate in the “BDC” region. We have not extended the voltage above 0.53 V, needed to reach the CO_2 region in this simple estimate.

6.2. First principles simulation of voltage-dependent electrochemistry in Li-ion batteries

The electrochemical processes that give rise to degradation processes, such as electrolyte reduction and SEI formation depend on the electrochemical potential at the battery electrodes. Modeling of electrochemistry under potential control is particularly difficult using density functional theoretical techniques that are based on electron charge density and not potential. In this work, we develop an approach to assign an absolute electrochemical scale to simulations using ab initio molecular dynamics (AIMD) and thermodynamic integration. [2] We apply the new technique to compute the free energy change for Li^+ transfer between a LiC_6 solid electrode and ethylene carbonate liquid electrolyte confined in a nanogap, ΔG_t . The onset of delithiation, at $\Delta G_t = 0$, is found to occur on LiC_6 anodes with negatively charged basal surfaces. These negative surface charges are evidently needed to retain Li^+ inside the electrode and should affect passivation (“SEI”) film formation processes. Fast electrolyte decomposition is observed at even larger electron surface densities. By assigning the experimentally known voltage (0.1 V vs Li^+/Li metal) to the predicted delithiation onset, an absolute potential scale is obtained. This enables voltage calibrations in simulation cells used in AIMD studies and paves the way for future prediction of voltage dependences in interfacial processes in batteries (see Figure 6.2).

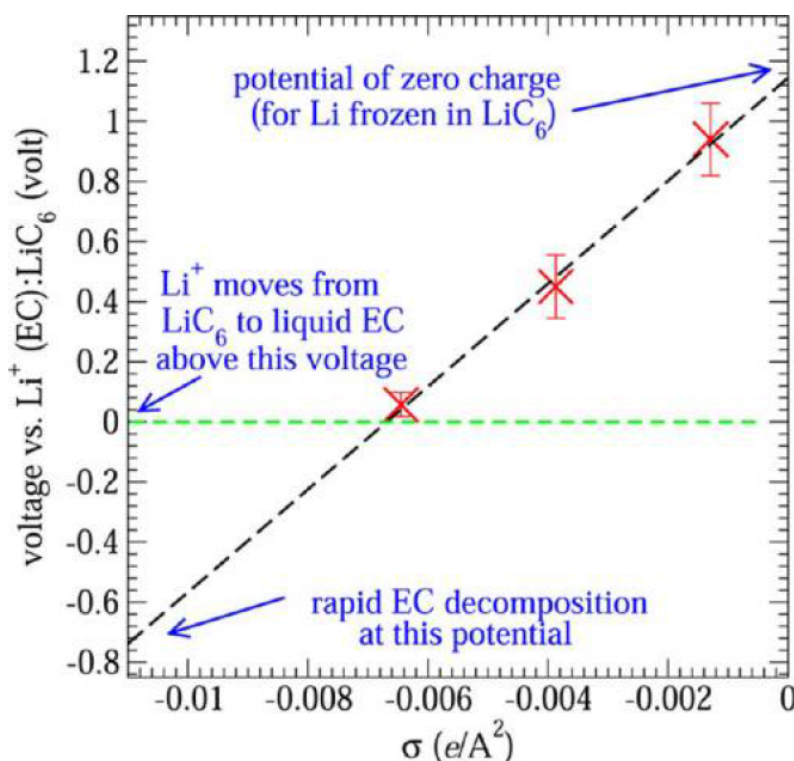


Figure 6.2. Predicted potential ($-\Delta G_t/e$) for virtual Li^+ transfer from the LiC_6 slab to the middle of the liquid EC region as the surface charge (σ) varies. Crosses denote the three data points computed, with 0, 1, and 2 mobile Li^+ , respectively. AIMD simulations with 4 mobile Li^+ and no counterions lead to EC decomposition.

6.3. References

1. K. Leung, "Two-electron reduction of ethylene carbonate: A quantum chemistry re-examination of mechanisms" *Chem. Phys. Lett.* **568-569**, 1 (2013).
2. K. Leung and C. M. Tenney, "Toward First Principles Prediction of Voltage Dependences of Electrolyte/Electrolyte Interfacial Processes in Lithium Ion Batteries," *J. Phys. Chem C* **117**, 24224 (2013).

7. ONGOING AND FUTURE WORK

Degradation mechanisms in Li-ion batteries are often specific to the materials chemistry of the battery anodes, cathodes, and electrolytes. The goal of this project was to develop new techniques that would provide knowledge of degradation mechanisms that are **broadly applicable** to a wide class of materials. In the first several sections, we described several novel characterization methods, such as in-situ TEM, STXM, TEM-compatible liquid cells, advanced electrochemical techniques, and first principles modeling of electrochemistry. In this section, we briefly highlight several additional characterization methods that represent current and ongoing work. As of the preparation of this report, investigations have been completed in some of these areas (noted as manuscripts in preparation). In other areas, proof-of-concepts have been demonstrated (noted as ongoing work).

7.1. In-situ TEM and STXM using Li-ion battery chemistry

In section 4 we described the development of a chip-based platform for performing electrochemical measurements inside a TEM. That work demonstrated the applicability of the technique, and current and ongoing work is focused on utilizing the platform for in-situ TEM and in-situ STXM measurements for the study of Li-plating at low electrode potentials, SEI formation on anodes, and the electrochemistry of cathodes. One example of this work is shown in Figure 7.1, which shows a series of TEM images of the plating and stripping of Li metal on a Ti electrode as the electrode is cycled under galvanostatic control in an ethylene carbonate-based battery electrolyte. [1] The in-situ TEM cell is also being used for in-situ STXM measurements. These experiments are the first demonstration of in-situ battery electrochemistry during STXM and represent a significant development in the field. The first experiment focused on the measurement of cycling behavior of a collection of LiFePO_4 particles in Li-ion battery electrolyte in order to understand the nucleation-controlled lithiation/delithiation process that was observed and discussed in section 3.[2] Figure 7.2 shows in-situ STXM images of LiFePO_4 particles taken near the Fe absorption edge (~ 700 eV). Preliminary work shows that the platform works, and future work is focused on collection of data for the LiFePO_4 system.

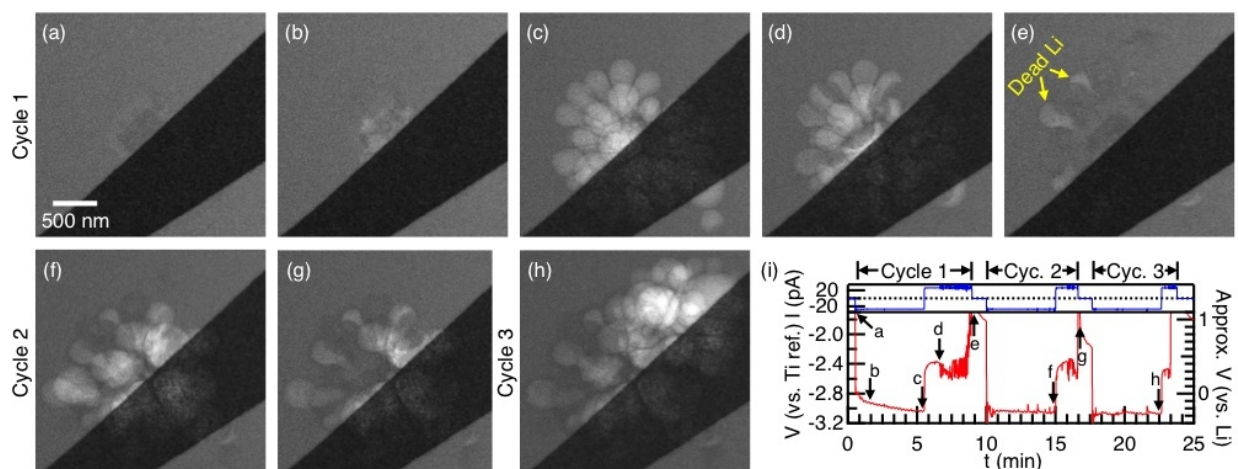


Figure 7.1. TEM of plating and stripping of Li metal on Ti electrodes in ethylene carbonate-based electrolyte. Three plating-stripping cycles are shown, as referenced in (i). The current density at the Ti electrode is 10 mA/cm^2 .

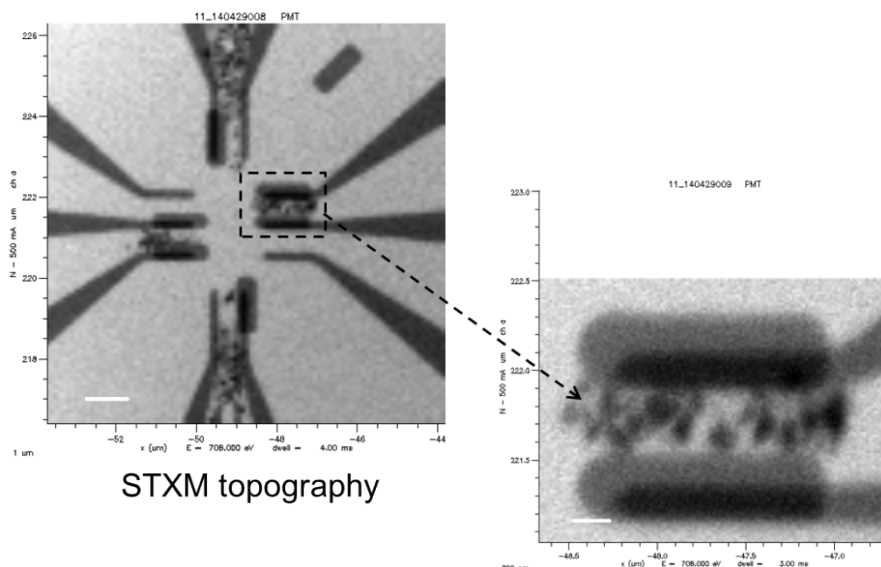


Figure 7.2. STXM image taken near the Fe absorption edge of LiFePO_4 particles in an ethylene carbonate-based electrolyte. The average particle size is 200 nm.

7.2. In-situ optical cells and optical characterization of flow batteries

Optical techniques provide an opportunity to probe the electrochemical reactions occurring inside a Li-ion battery, provided there is an optical window in the cell. During this project an in-situ optical cell was designed for the Raman spectroscopy measurement of Li-ion battery reactions at cathodes, see Figure 7.3. During the development of the optical cell, one of the principal challenges was the low transparency of the ethylene carbonate-based electrolytes at conventional Raman excitation wavelengths, 532 nm, due to a high fluorescence background. However, it was soon discovered that this in-situ Raman cell is ideally suited for the study of redox flow batteries which are typically based on aqueous electrolytes. An early application of this optical cell was applied for the study of vanadium trisdithiolene redox flow batteries wherein the reduction and oxidation products are monitored in real-time during several charge-discharge cycles (see Figure 7.4).[3]

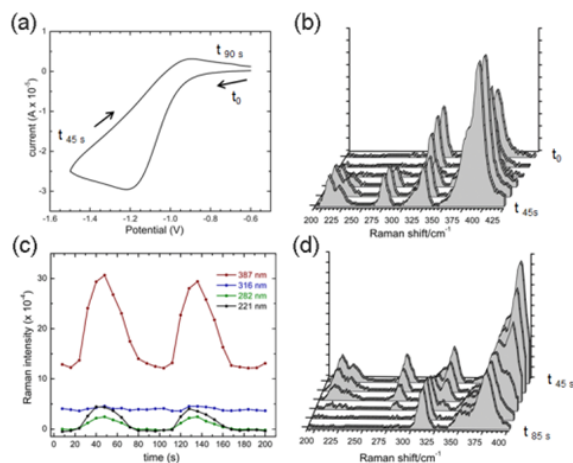
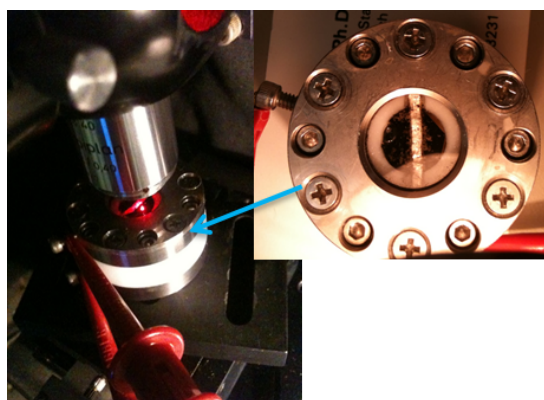


Figure 7.3. An in situ optical cell for Raman spectroscopy of batteries.

Figure 7.4. In situ Raman spectroscopy of vanadium trisdithiolene flow batteries. (a) Cyclic voltammetry and (b)-(d) the variation in Raman peak intensity and Raman spectra over time while the flow battery is cycled.

7.3. Degradation studies of $\text{LiNi}_{0.5}\text{Co}_{0.2}\text{Mn}_{0.3}\text{O}_2$

$\text{LiNi}_{0.5}\text{Co}_{0.2}\text{Mn}_{0.3}\text{O}_2$ (NMC 532) is an increasingly popular cathode for the commercial development of Li-ion batteries due to its low cost compared to LiCoO_2 , its relatively high voltage (~ 4 V), and its good cycle life. In this project, we initiated several experiments to understand the behavior and degradation of NMC 532. In contrast to LiFePO_4 , NMC 532 is a more challenging cathode for study due to the co-existence of several transition metal ions that can undergo oxidation and reduction and due to the chemistry of the lithiation and delithiation process, which is an insertion reaction as opposed to a phase change reaction. STXM experiments were performed on slices of NMC 532 ultramicrotomed from battery cathodes that were cycled and polarized to several states-of-charge, including fully charged, fully discharged, and 50% charged.[4] Figure 7.5 shows some examples of early STXM measurements including attempts to map a 50% state-of-charge (SOC) cathode as a mixture of fully charged and discharged reactions. The x-ray absorption spectra for the Ni, Mn, Co, and O components have a complicated dependence on the oxidation state and local environment of the ions. The local environment of the transition metal ions is highly variable, as the Ni and Mn and Co ions are randomly ordered on the cation sublattice. In order to understand the spectral components of the x-ray absorption spectra, a modelling and simulation effort has been undertaken consisting of (a) first principles calculations of the relaxed structure for a large number of $12 \times 12 \times 6$ unit cells of $\text{LiNi}_{0.5}\text{Co}_{0.2}\text{Mn}_{0.3}\text{O}_2$ with random ordering of the cations (see Figure 7.6) combined with (b) simulated x-ray absorption spectra.[5]

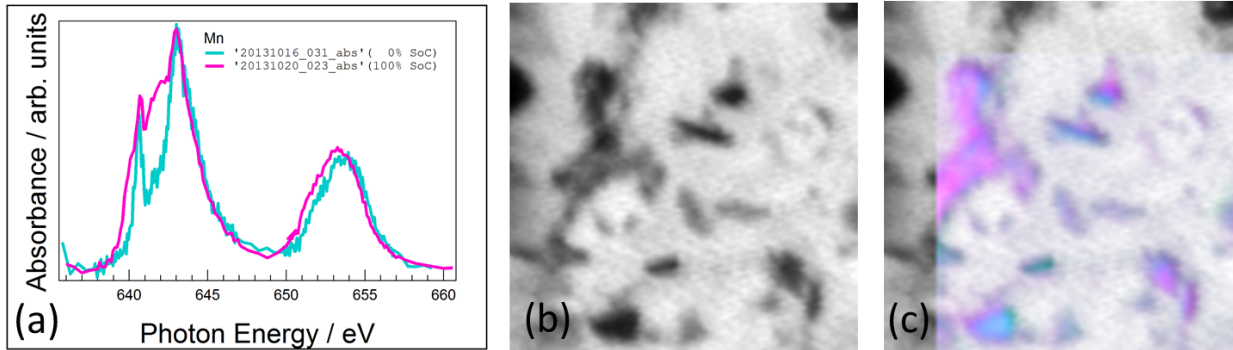


Figure 7.5. (a) X-ray absorption spectra near the Mn absorption edge for fully charged (pink) and fully discharged (blue) $\text{LiNi}_{0.5}\text{Co}_{0.2}\text{Mn}_{0.3}\text{O}_2$ cathodes, (b) a STXM image of a $\text{LiNi}_{0.5}\text{Co}_{0.2}\text{Mn}_{0.3}\text{O}_2$ cathode at 50% SOC, and (c) spectral fits of the 50% SOC sample into fully-charged (pink) and fully-discharged (blue) components. Mean particle size is approximately one micron.

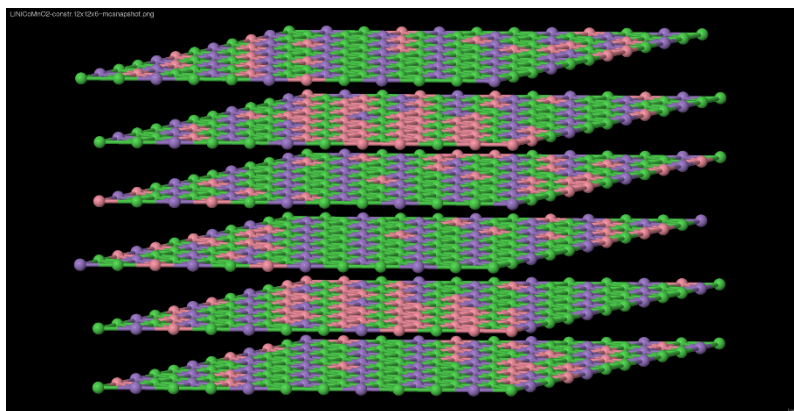


Figure 7.6. A simulation cell of 6 layers of $\text{LiNi}_{0.5}\text{Co}_{0.2}\text{Mn}_{0.3}\text{O}_2$ displaying one arrangement of Ni (green), Co (pink), and Mn (purple) ions.

Degradation studies were also performed on NMC 532, focusing on the effect of high voltage charging on cathode performance. At charging potentials at or above 4.4V, capacity loss is observed and distinct features are observed in the Raman spectra, including a change in spectral line shape and a shift in the primary peak to above 600 cm^{-1} . These spectral features are similar to the Raman spectral features of the spinel phase of LiMnO_2 , suggesting that a phase change may be occurring – at least in the near surface region. Raman spectral maps were recorded for these degraded cathodes to map the distribution of particles that show the altered Raman spectra in order to see the extent and distribution of the altered cathode (see Figure 7.7).[6]

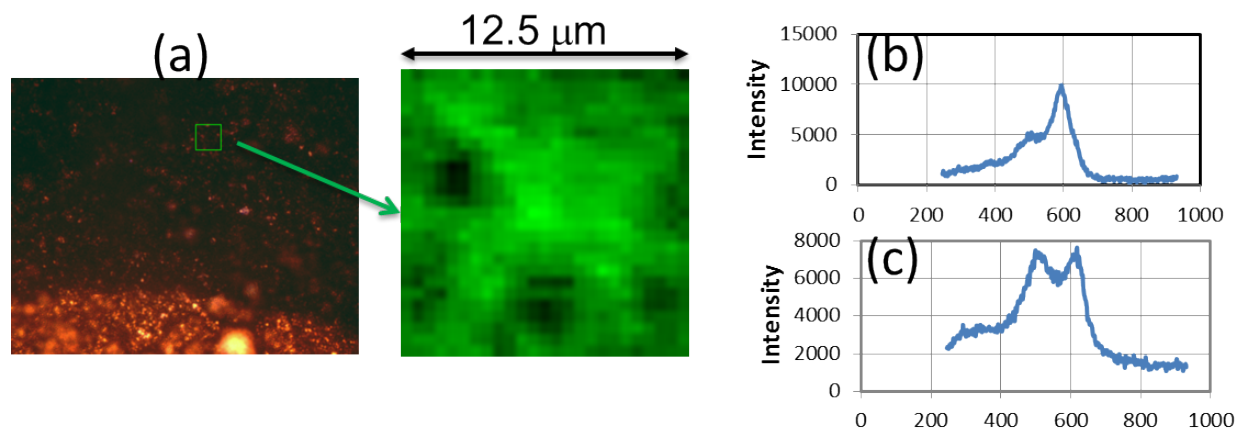


Figure 7.7. (a) Raman map of $\text{LiNi}_{0.5}\text{Co}_{0.2}\text{Mn}_{0.3}\text{O}_2$ that has been charged to 4.4 V to introduce degradation. The map is spectrally filtered on the Raman component above 600 cm^{-1} , which appears as a result of high voltage charging (c) but is not present in the material cycled to lower voltage (b). This high voltage degradation component is heterogeneously distributed.

We expect that the work represented in this section will be completed and published in calendar year 2015.

7.4. References

1. A. J. Leenheer, K. L. Jungjohann, K. R. Zavadil, J. P. Sullivan, and C. T. Harris, "Lithium electrodeposition dynamics imaged in-situ by liquid cell scanning transmission electron microscopy," manuscript in preparation, 2014.
2. F. El Gabaly, A. H. McDaniel, T. Tyliczszak, K. R. Fenton, A. J. Leenheer, and C. T. Harris, "In Situ STXM of LiFePO_4 ," ongoing work, 2014.
3. A. Talin and M. Anstey, "In situ Raman of a Vanadium Trisdithiolene redox flow battery," manuscript in preparation, 2014.
4. F. El Gabaly, A. H. McDaniel, T. Tyliczszak, W. C. Chueh, K. R. Fenton, and J. D. Sugar, "STXM studies of $\text{LiNi}_{0.5}\text{Co}_{0.2}\text{Mn}_{0.3}\text{O}_2$," ongoing work, 2014.
5. A. H. McDaniel, C. M. Tenney, and K. Leung, "X-ray absorption analysis of $\text{LiNi}_{0.5}\text{Co}_{0.2}\text{Mn}_{0.3}\text{O}_2$ as a function of state-of-charge," ongoing work, 2014.
6. C. Hayden, and A. A. Talin, "Raman spectroscopic analysis of $\text{LiNi}_{0.5}\text{Co}_{0.2}\text{Mn}_{0.3}\text{O}_2$ cathodes stressed to high voltage," manuscript in preparation, 2014.

APPENDIX A: SUPPLEMENTAL INFORMATION ON SANDIA'S IN-SITU TEM LIQUID CELL

A.1. The Liquid Cell Discovery Platform: Imaging Electrochemical Processes in the Transmission Electron Microscope

A.1.1. Epoxy wicking to seal ring

The seal ring was designed to define the boundaries of the liquid chamber, and during assembly the epoxy wicked between the two chips up to the seal ring as shown in Figure S1. Epoxy residue is visible outside the seal ring, but no epoxy entered the area inside the seal ring.

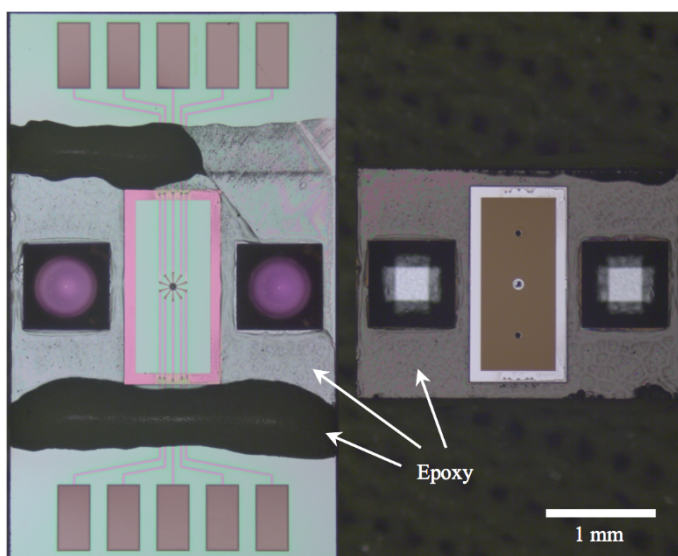


Figure S1. Optical microscope image of bottom (left) and top (right) chips after partial epoxy cure and subsequent disassembly using a razor blade.

A.1.2. Fabrication workflow

A schematic cell fabrication workflow for the bottom chip containing electrodes is shown in Figure S2.

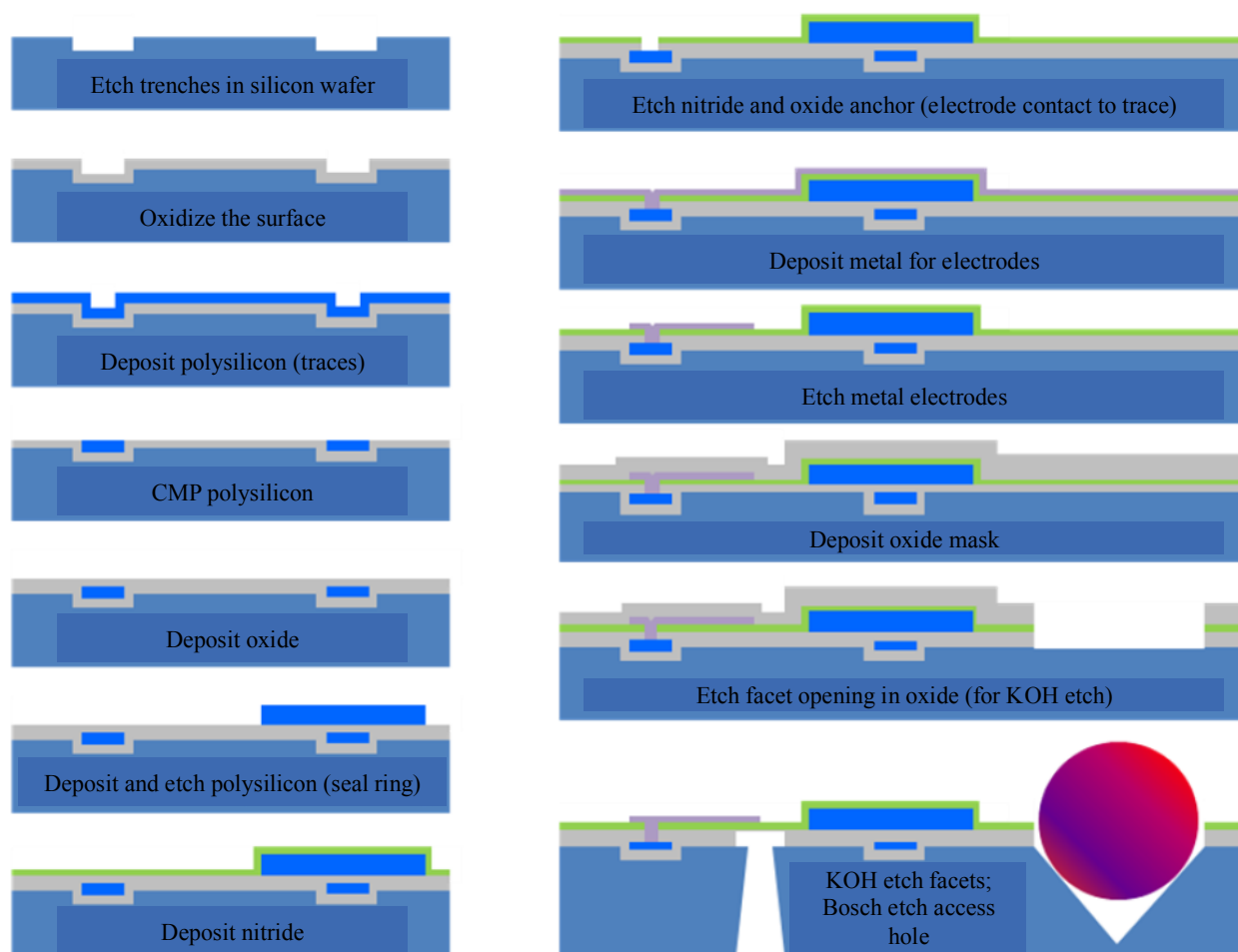


Figure S2. Microfabrication steps used to fabricate the bottom chip of the liquid cell.

A similar but simpler fabrication scheme was used to make the lids where no metal electrodes were required.

A.1.3. Post-processing lithography

To insulate the bulk of the metal electrodes, an ALD Al_2O_3 layer was deposited over the top surface of the bottom chip using 300 cycles of trimethylaluminum gas and water vapor at 200 °C resulting in a conformal film thickness of about 33 nm. Electron beam lithography was performed using spincoated 950K PMMA resist followed by an HF-based etch to remove the Al_2O_3 ; however, the PMMA was found to easily delaminate in the wet HF etch, so an additional 7-nm thick SiO_2 layer was deposited on the Al_2O_3 by sputtering to increase the PMMA adhesion. The wet etch consisted of 2 parts ethylene glycol : 1 part buffered oxide etch (6:1) which etched both oxides at roughly 1 nm/s but did not attack the metal electrodes.

A.1.4. Cell liquid filling

Photographs of the an assembled cell during the filling procedure are shown in Fig. S3. After placing a small piece of standard Scotch tape over the center view port (Fig. S3(a)) to ensure liquid did not contaminate the nitride window, a droplet of liquid was placed at one of the fill ports using a fine-tipped micropipette. Excess liquid was wicked away using a cleaning tissue, leaving some liquid in the chamber and fill port. The Scotch tape was removed, and a piece of

polyimide tape was placed over both fill ports (Fig. S3(b)). If necessary to prevent vapor exchanged with the atmosphere or TEM environment, quick-set epoxy was spread over the top surface, avoiding the view port (Fig. S3(c)).

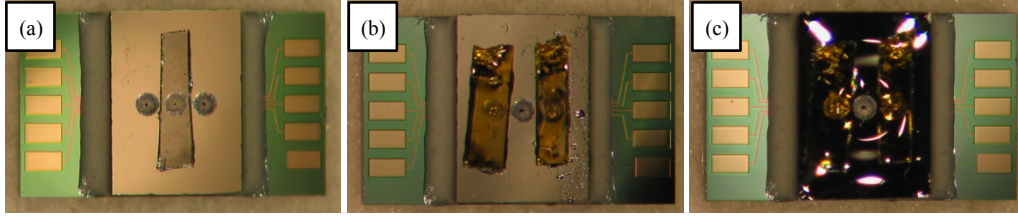


Figure S3. A fully-assembled liquid cell being filled with liquid. (a) Protective clear tape over center view port; (b) polyimide tape over the fill ports after liquid filling; (c) clear epoxy over the lid everywhere except the view port.

A.1.5. Electron beam energy loss in liquid

An incident electron loses energy as it passes through a liquid layer, and the loss per distance (stopping power) is given by the Bethe formula [1], [2],

$$-\frac{dE}{dz} = \frac{2\pi N e^4 Z_{eff} \ln(1.1658E/I)}{(4\pi\epsilon_0)^2 E},$$

where E is the electron energy, z is the distance, N is the number of atoms per unit volume, e is the electric charge, Z_{eff} is the liquid's effective atomic number, I is the liquid's mean ionization potential, and ϵ_0 is the permittivity of free space (using SI units). The effective atomic number is calculated by $Z_{eff} = \sum_i f_i Z_i^{1.3} / \sum_i f_i Z_i^{0.3}$ where f_i is the atomic fraction of atom i , and the mean ionization potential in eV is approximated for $Z < 13$ by $I = Z(12 + 7/Z)$ [3]. For water, $Z_{eff} = 4.38$ and $I = 60$ eV, thus for a 300-keV incident electron, $-dE/dZ = 0.17$ eV/nm. Alternatively, the tabulated value for liquid water based on mass fractions is 0.24 eV/nm [4]. Therefore in a liquid layer of thickness 100 to 1000 nm, the incident electron can lose tens to hundreds of eV on average. The energy loss will increase with density or atomic weight, but most liquid electrolytes including organic solvents will have similar values.

The energy loss *per collision* can be estimated based on the inelastic scattering cross sections combined with the above stopping power. The mean energy loss (\bar{E}) per inelastic scattering collision is given by

$$\bar{E} = \frac{dE/dz}{N\sigma_i}$$

where the inelastic cross section σ_i for low- Z elements is of order 10^{-4} nm² [3]. Thus for water, $\bar{E} \sim 20$ eV per collision.

A.2. References

- [1] J. R. Breedlove and G. T. Trammell, "Molecular Microscopy: Fundamental Limitations," *Science*, vol. 170, no. 3964, pp. 1310–1313, Dec. 1970.
- [2] H. Zheng, S. A. Claridge, A. M. Minor, A. P. Alivisatos, and U. Dahmen, "Nanocrystal Diffusion in a Liquid Thin Film Observed by in Situ Transmission Electron Microscopy," *Nano Lett.*, vol. 9, no. 6, pp. 2460–2465, Jun. 2009.
- [3] R. F. Egerton, *Electron Energy-Loss Spectroscopy in the Electron Microscope*, 3rd ed. New York: Springer Berlin Heidelberg, 2011.
- [4] M. J. Berger, J. S. Coursey, M. A. Zucker, and J. Chang, "ESTAR, PSTAR, and ASTAR: Computer Programs for Calculating Stopping-Power and Range Tables for Electrons,

Protons, and Helium Ions,” *physics.nist.gov*. National Institute of Standards and Technology, Gaithersburg, MD.

DISTRIBUTION

1	MS0613	Tom Wunsch	2546
1	MS0885	Doug Wall	1810
1	MS0887	Terry Aselage	1800
1	MS1108	Sean Hearne	6111
1	MS1415	Carlos Gutierrez	1114
1	MS9161	Sarah Allendorf	8340
1	MS9161	John Sullivan	8340
1	MS0899	Technical Library	9536 (electronic copy)
1	MS0359	D. Chavez, LDRD Office	1911

